

THE *Swift* BAT PERSPECTIVE ON NON-THERMAL EMISSION IN HIFLUGCS GALAXY CLUSTERSDANIEL R. WIK^{1,6}, CRAIG L. SARAZIN², YU-YING ZHANG³, WAYNE H. BAUMGARTNER¹, RICHARD F. MUSHOTZKY⁴, JACK TUELLER¹, TAKASHI OKAJIMA¹, AND TRACY E. CLARKE⁵

Draft version July 4, 2012

ABSTRACT

The search for diffuse non-thermal, inverse Compton (IC) emission from galaxy clusters at hard X-ray energies has been underway for many years, with most detections being either of low significance or controversial. In this work, we investigate 14–195 keV spectra from the *Swift* BAT all sky survey for evidence of non-thermal excess emission above the exponentially decreasing tail of thermal emission in the flux-limited HIFLUGCS sample. To account for the thermal flux contribution at BAT energies, *XMM-Newton* EPIC spectra are extracted from coincident spatial regions so that both the thermal and non-thermal spectral components can be determined simultaneously. We find marginally significant IC components in 6 clusters, though after closer inspection and consideration of systematic errors we are unable to claim a clear detection in any of them. The spectra of all clusters are also summed to enhance a cumulative non-thermal signal not quite detectable in individual clusters. After constructing a model based on single temperature fits to the *XMM-Newton* data alone, we see no significant excess emission above that predicted by the thermal model determined at soft energies. This result also holds for the summed spectra of various subgroups, except for the subsample of clusters with diffuse radio emission. For clusters hosting a diffuse radio halo, relic, or mini-halo, non-thermal emission is initially detected at the $\sim 5\sigma$ confidence level, but modeling and systematic uncertainties ultimately degrade this significance. This marginal detection is driven by the mini-halo subgroup, suggesting low average magnetic field strengths ($B \sim 0.1\mu\text{G}$) in the cores of these clusters.

Subject headings: galaxies: clusters: general — intergalactic medium — magnetic fields — radiation mechanisms: non-thermal — X-rays: galaxies: clusters

1. INTRODUCTION

A number of observations, mainly at radio frequencies, have established that relativistic particles and magnetic fields are part of the intracluster medium (ICM) of galaxy clusters (e.g., Govoni & Feretti 2004). The large ($\sim\text{Mpc}$) scale, diffuse structures known as radio halos and relics are produced by relativistic electrons spiraling around $\sim\mu\text{G}$ magnetic fields. Because halos and relics are not detected in every cluster, but are only found in clusters with ongoing major merger activity (Buote 2001; Schuecker et al. 2001), mergers probably temporarily reaccelerate underlying relativistic populations (e.g., Sarazin 1999; Brunetti & Blasi 2005). It is important to fully characterize the non-thermal phase if the dynamics and general state of the ICM is to be understood; the proportion of energy tied up in these relativistic components, if significant, may bias inferred mass estimates necessary to use clusters as cosmological probes (e.g., Mantz et al. 2008; Vikhlinin et al. 2009; Vanderlinde et al. 2010). Unfortunately, synchrotron emission alone cannot separately determine particle and magnetic field energy densities, and so the total energy in

the non-thermal phase remains relatively unconstrained. However, the electron population can be independently observed through inverse Compton (IC) emission due to scattering of the ubiquitous Cosmic Microwave Background (CMB) photons, which are up-scattered to X-ray energies and may be observable if the electron population is sufficiently large (Rephaeli 1979). Detections of IC emission, therefore, have the potential to determine whether the non-thermal phase is energetically negligible or, particularly if the average magnetic field is large, it is sizable enough to affect the dynamics and structure of the thermal gas.

Thermal emission clearly dominates at $\sim\text{keV}$ energies, so searches for excess emission due to an IC spectral component are more easily undertaken at very soft or hard ($> 10\text{ keV}$) energies. The latter range is particularly promising, given the exponential decline in the thermal spectrum and the lack of Galactic and solar wind charge exchange foregrounds that can hamper searches at soft energies (Koutroumpa et al. 2009; Takei et al. 2007; Bonamente et al. 2009). In particular, the *Swift* BAT all sky survey (Tueller et al. 2010) provides a deep map of hard energy (14–195 keV) emission from which non-thermal excesses can be identified. Its uniform coverage and impressive sensitivity makes it the most complete dataset from which to study the brightest objects in a given class (e.g., Winter et al. 2009). Whereas previous searches have concentrated on long pointed observations of individual clusters, this survey allows a larger, more uniform sample to be searched, as similarly done by Ajello et al. (2009, 2010) for detected BAT clusters. To take full advantage of this capability, we have chosen the

¹ Astrophysics Science Division, NASA/Goddard Space Flight Center, Greenbelt, MD 20771, USA; daniel.r.wik@nasa.gov

² Department of Astronomy, University of Virginia P. O. Box 400325, Charlottesville, VA 22904-4325

³ Argelander-Institut für Astronomie, Universität Bonn, Auf dem Hügel 71, 53121 Bonn, Germany

⁴ Department of Astronomy, University of Maryland, College Park, MD 20742, USA

⁵ Naval Research Laboratory, 4555 Overlook Ave. SW, Code 7213, Washington, DC 20375, USA

⁶ NASA Postdoctoral Program Fellow

flux-limited HIFLUGCS sample (Reiprich & Böhringer 2002), which contains the brightest clusters in the sky outside the Galactic plane. The selection of the brightest clusters may provide the greatest opportunity to detect IC emission, as in most models the nearest and most luminous clusters are expected to have the strongest IC signal. Also, because these clusters are bright and contained within a well-defined survey, there already exist good observations at lower X-ray energies, which can be used to strongly constrain the thermal properties of the ICM – an important prerequisite for the robust detection of an IC excess. Finally, the fact that HIFLUGCS is a complete flux-limited survey allows one to discuss the statistical properties of their hard excesses by stacking the individual cluster observations.

Because they are nearby and bright, many of the clusters in HIFLUGCS have been targets of IC searches with other telescopes, including A3667 (Finoguenov et al. 2010), A3112 (Bonamente et al. 2007), A3376 (Kawano et al. 2009), A2256 (Fusco-Femiano et al. 2005), A1367 (Henriksen & Mushotzky 2001), A2199 (Kempner & Sarazin 2000), and A2163 (Rephaeli et al. 2006). Most often clusters are targeted because they host a radio halo or relic, as the IC flux then leads to a direct measure of the average magnetic field strength. A large fraction of HIFLUGCS clusters were also included in an analysis of all long exposure *Beppo-SAX* observations (Nevalainen et al. 2004), which found marginal evidence for non-thermal excesses in individual clusters but a substantial excess in a stacked spectrum. In general, an IC component distinct from thermal emission in the hard band has been difficult to clearly identify, with perhaps the only counter example being an exceptionally deep observation of the Ophiuchus cluster (Eckert et al. 2008). The cluster most thoroughly searched for non-thermal emission, also in HIFLUGCS, is the Coma cluster. Controversial (Rossetti & Molendi 2004) detections with *RXTE* (Rephaeli & Gruber 2002) and *Beppo-SAX* (Fusco-Femiano et al. 2004) have recently been challenged with comparable *Suzaku* (Wik et al. 2009) observations and a detailed analysis of the *Swift* BAT survey data (Wik et al. 2011).

To perform the deepest hard X-ray survey of non-thermal emission in clusters to date, we jointly fit high quality *XMM-Newton* EPIC and *Swift* BAT spectra, extracted from identical regions and cross-calibrated to make their absolute spectral responses as consistent as possible. We describe the data and its calibration in Section 2. In Section 3, the thermal and non-thermal character of the spectra are separately analyzed, and in Section 4 they are jointly fit for each individual cluster. We also search for a statistical hard excess in sets of stacked spectra for the entire sample and for several subsamples in Section 5. Lastly, the implications of our results are discussed in Section 6. We assume a flat cosmology with $\Omega_M = 0.23$ and $H_0 = 70 \text{ km s}^{-1} \text{ Mpc}^{-1}$. Unless otherwise stated, all uncertainties are given at the 90% confidence level.

2. OBSERVATIONS AND DATA PREPARATION

2.1. *XMM-Newton* EPIC Spectra

For the lower energy BAT bands, it is very useful to have X-ray spectra at lower energies to constrain the

thermal emission; this is particularly true given that the *Swift* BAT survey spectra are coarsely binned (8 channels spanning $14 \text{ keV} < E < 195 \text{ keV}$). Also, any non-thermal component in the BAT spectra must be consistent with the spectra at softer energies. *XMM-Newton* is the ideal observatory to provide such complementary spectra. For one, its large field of view (FOV) allows a higher fraction of the total emission, which can be quite extended given the low redshifts of the sample, to be detected in a single pointing. Additionally, the EPIC instruments are sensitive to 5–10 keV photons, which make them more useful for constraining the highest temperature gas, and the telescopes have good spatial resolution so that point sources can be excluded from the spectra. Last, but of no less importance, *XMM-Newton* has observed all but one (Abell 2244) of the clusters in HIFLUGCS. Unfortunately, another 4 cluster observations (Abell 401, Abell 478, Abell 1736, and Abell 2163) are heavily contaminated by background flares and consequently unusable (for more details, see Zhang et al. 2011). However, the data for the remaining 59 clusters are of sufficient quality to help constrain potential non-thermal signals in the BAT energy bands.

We extract *XMM-Newton* spectra for each cluster from the largest circular region that either covers the FOV or extends to the point where cosmic X-ray background (CXB) emission begins to dominate, by summing the annular spectra from Zhang et al. (2009). To ensure near Gaussian statistics for χ^2 fitting, adjacent channels are grouped until each new bin contains at least 30 counts. The centers and radii of the circular regions, along with each pointing’s observation ID, are listed in Table 1. Source spectra are extracted in concentric annuli within the region; corresponding particle background spectra are derived from CLOSED mode calibration data, which are renormalized based on 3–10 keV events out of the FOV and outside of a $15'.4$ radius from the detector center (for details see Section 2.4 of Zhang et al. 2009). The full background treatment is described in Zhang et al. (2009). As an additional step, we readjust the normalization of the particle background spectra by hand to ensure the 7–12 keV continuum of the cluster spectra have a more physical shape. We define “more physical” as the background normalization that minimizes the χ^2 statistic for a single temperature (1T) (using the APEC plasma emission model⁷) individually fit to the EPIC-pn ($2 < E < 12 \text{ keV}$) and MOS1 and MOS2 ($2 < E < 10 \text{ keV}$) spectra. The new best-fit temperatures, after these initial renormalizations of the background, are compared to each other and to previous measurements (primarily Reiprich & Böhringer 2002). While this method may bias the background level, especially if a single temperature model is a poor description of a given spectrum, repeating this procedure with two temperature (2T) and single temperature plus power law (T+NT) models yield comparable or inferior results, usually favoring obvious under-subtractions of the background that produce systematic patterns in the residuals. We favor normalizations that leave the background slightly under-subtracted, in order to avoid removing a real non-thermal signature. For the most part, the overall spectrum is only mildly affected since much of the

⁷ http://cxc.harvard.edu/atomdb/sources_apec.html

emission is at lower energies where the background is a smaller fraction of the total. One consequence is that instrumental lines, which are typically between 7.5 and 9.5 keV and mainly are a problem in the EPIC-pn spectra and which can vary in intensity relative to the background continuum, can be under- or over-subtracted. No resolved ICM lines exist in this range, so we simply ignore this energy range when poor line subtractions occur, as in Wik et al. (2009). Based on the change in χ^2 as the background normalization is varied, a typical 90% level uncertainty in the normalization is $\sim 3\%$.

We choose to model, instead of subtract, one further background component: the CXB due to extragalactic sources. Lumb et al. (2002), using *XMM-Newton* sky fields, find that this component of the CXB is well fit by a power law with photon index of 1.42 in the hard band (2–10 keV). Their results are in good agreement with other work in this band (e.g., Moretti et al. 2003; De Luca & Molendi 2004). We adopt their normalization at 1 keV of $8.44 \text{ photons cm}^{-2} \text{ s}^{-1} \text{ keV}^{-1} \text{ sr}^{-1}$, which is scaled to match the extraction area for each cluster. The impact of cosmic variance, or the field-to-field variation in CXB flux resulting from large scale structure and source population selection, is not included as a systematic uncertainty in the following analysis due to its small effect. While cosmic variance increases with decreasing solid angle, the high sensitivity of *XMM-Newton* allows most of the sources responsible for a higher variance to be removed, so for one of our typical regions the 90% uncertainty is only $\sim 10\%$ of the CXB flux. Note that Lumb et al. (2002) remove detected point sources as is done here, so their spectrum can be directly applied as is. The Galactic component of the CXB is also not considered, as it only contributes below 1 keV, and we restrict our fits to the 2–12 keV range.

2.2. *Swift* BAT 58-month Survey Spectra

The *Swift* mission and the properties of the survey are described in detail in Wik et al. (2011, Section 2.2) and in Tueller et al. (2010). Similarly, we refer to that Section and the appendices for details on the extraction and calibration of sources from survey image data. To briefly summarize, the flux calibration is tied to the Crab spectrum, which we define to have the same spectrum as that observed by *XMM-Newton* for $E > 2$ keV, extrapolated to BAT energies via an adopted model based on *Suzaku* observations. In this way, both the cross-normalization and spectral shape of the *XMM-Newton* and *Swift* spectra will match, and continuous models can be jointly fit to them simultaneously. Unfortunately, independent measurements by various instruments, including the *Swift* BAT, have recently demonstrated that the hard X-ray spectrum of the Crab is in fact variable on yearly timescales (Wilson-Hodge et al. 2011). At 14–50 keV energies, where the only appreciable amount of flux is detected from clusters, the variation spans about 10% over the last 5 years, with a consistent decline only over the last 2 years (see Fig. 5 of Wilson-Hodge et al. 2011). Our flux calibration of BAT sources depends on an adopted model for the Crab spectrum, which is taken from *Suzaku* XIS and HXD-PIN observations that took place in August 2005; this time occurs during one of the higher flux periods. Since the BAT survey spectrum of the Crab spans the following 5 years of observations

TABLE 1
XMM-Newton OBSERVATIONS, REGIONS, AND CLUSTER CLASSES

Name	ObsID	α (J2000) (deg)	δ (J2000) (deg)	Radius (arcmin)	Class ^a
A0085	0065140101	10.45957	-9.30303	11.6667	SCC
A0119	0505211001	14.07130	-1.25327	9.3333	NCC
A0133	0144310101	15.67971	-21.87968	6.7000	SCC
NGC507	0080540101	20.91068	33.25063	9.4667	SCC
A0262	0109980101	28.19002	36.15114	13.5333	SCC
A0400	0404010101	44.42226	6.02696	12.6667	NCC
A0399	0112260101	44.46513	13.04713	10.4000	NCC,R
A3112	0105660101	49.49456	-44.23562	6.9667	SCC
Fornax	0400620101	54.61989	-35.45122	10.6333	SCC
2A0335	0109870101	54.66787	9.96803	8.9667	SCC,R
IIIZw54	0505230401	55.32801	15.40390	6.8667	WCC
A3158	0300211301	55.72316	-53.63099	9.1333	NCC
NGC1550	0152150101	64.90839	2.40929	11.6667	SCC
EXO0422	0300210401	66.46339	-8.56118	7.1333	SCC
A3266	0105260901	67.81198	-61.44835	12.0000	WCC
A0496	0135120201	68.40753	-13.26069	10.1667	SCC
A3376	0151900101	90.54203	-39.95994	6.0000	NCC,R
A3391	0505210401	96.60081	-53.69002	6.7333	NCC
A3395s	0400010301	96.69188	-54.54530	4.2000	NCC
R1504	0401040101	106.37174	-12.93125	8.1992	SCC,R
A0576	0205070301	110.35886	55.75948	9.0000	WCC
A0754	0136740101	137.32574	-9.68781	10.1667	NCC,R
HydraA	0109980301	139.52491	-12.09342	5.0000	NCC
A1060	0206230101	159.17853	-27.52841	8.4667	WCC
A1367	0061740101	176.18539	19.73211	10.0000	NCC,R
MKW4	0093060101	181.11522	1.89480	8.3333	SCC
ZwCl1215	0300211401	184.41928	3.65818	6.2333	NCC
NGC4636	0111190701	190.70940	2.69179	9.8333	SCC
A3526	0406200101	192.21101	-41.30430	12.9333	SCC
A1644	0010420201	194.29469	-17.40291	14.7333	SCC
A1650	0093200101	194.67448	-1.75920	5.1667	WCC
A1651	0203020101	194.84310	-4.19633	7.5000	WCC
Coma	0124711401	194.93888	27.95150	14.6667	NCC,R
NGC5044	0037950101	198.84908	-16.38664	11.5000	SCC
A3558	0107260101	202.00169	-31.50027	10.2333	WCC
A3562	0105261801	203.40201	-31.67382	6.1667	WCC,R
A3571	0086950201	206.86609	-32.86052	8.5000	WCC
A1795	0097820101	207.21991	26.59282	8.0000	SCC
A3581	0205990101	211.87760	-27.01320	11.0667	SCC
MKW8	0300210701	220.17560	3.47159	7.5667	NCC
A2029	0111270201	227.73326	5.74264	6.5000	SCC,R
A2052	0109920101	229.18501	7.02012	7.0667	SCC
MKW3S	0109930101	230.45945	7.70323	9.6667	SCC
A2065	0112240201	230.62112	27.72063	6.6667	WCC
A2063	0550360101	230.77401	8.60701	7.1667	WCC
A2142	0111870301	239.56451	27.25178	6.6667	WCC,R
A2147	0505210601	240.56789	15.97177	11.3333	NCC
A2199	0008030201	247.15461	39.54811	12.3333	SCC
A2204	0112230301	248.19604	5.57554	6.1333	SCC,R
A2256	0141380201	255.96829	78.67197	8.0000	NCC,R
A2255	0112260801	258.22709	64.06428	8.1667	NCC,R
A3667	0206850101	303.16966	-56.84081	13.0000	WCC,R
S1101	0123900101	348.49294	-42.72664	6.0333	SCC
A2589	0204180101	350.98652	16.77595	5.0000	WCC
A2597	0147330101	351.33334	-12.12416	6.5667	SCC
A2634	0002960101	354.62099	27.03107	11.0000	WCC
A2657	0402190301	356.23640	9.19810	5.6667	WCC
A4038	0204460101	356.93602	-28.14506	12.3333	WCC
A4059	0109950201	359.25704	-34.75803	9.1333	SCC

^a From Hudson et al. (2010): SCC = “strong cool core cluster,” WCC = “weak cool core cluster,” and NCC = “non-cool core cluster”; clusters that host a radio halo and/or relic are labeled with “R”

and averages over these fluctuations, the normalization of our adopted model is only 2-3% higher than the actual flux emitted. The effect this has on our derived fluxes is to make them 2-3% higher than they actually are; this amount is equivalent to the 1σ error on the 14–20 keV flux of Coma, which is the highest signal-

to-noise flux considered here by a factor of 2. Also, Wilson-Hodge et al. (2011) show that the recent decline in flux is more dramatic for higher energy bands. Both of these behaviors – the overall decline in flux and the steepening of the spectrum – bias our derived BAT fluxes high, which could lead to a higher chance of false non-thermal detections. However, since we find no convincing evidence for non-thermal excesses even given this probable effect, and since we allow for a 10% cross-calibration uncertainty between the BAT and EPIC spectra, which easily encompasses this level of variability, it is clear that our choice of flux calibrator does not strongly impact the following analysis, except to make our upper limits slightly more conservative than they otherwise would be.

While the standard processing of coded mask imaging data is designed to extract the fluxes of point sources, it is also possible to extract the flux of a mildly extended source, albeit with somewhat greater uncertainty (Renaud et al. 2006; Wik et al. 2011). The large effective PSF (full width at half maximum FWHM $\sim 20'$) for point sources in the survey means that even nearby clusters of galaxies will appear only slightly extended; the FWHM of the Coma cluster – the most extended, reliably detected source in the survey – is only $28'.5$. Note that while 4 clusters (Fornax, NGC 4636, A3526, and A1060) have larger angular extents than Coma (based on angular R_{500} estimates, Eckert et al. (2011)), they are all cooler, less massive systems and thus either not detected or only marginally detected by the BAT at 14–20 keV. From Figure 1, it is clear that detected clusters (colored circles) are typically extended, relative to other sources. The horizontal lines mark the standard deviation of best-fit FWHM values for the non-cluster sources in each signal-to-noise bin; they also represent the approximate error on FWHM estimates for the clusters in each bin. Individual clusters are labeled in the 4 lowest energy BAT bands when they are detected at a signal-to-noise ratio greater than 5. We follow the procedure outlined in Wik et al. (2011) to extract fluxes for diffuse sources, which requires the spatial distribution of the emission to be known. Because clusters are comparable in size to the effective spatial resolution of the survey, detailed spatial models are not necessary to extract accurate fluxes. We consider generic β -model surface brightness profiles, which well represent the radial profiles at softer energies. Taking a representative value for β of 0.75, we find that all $> 3\sigma$ detected clusters (in a given band) can be well fit with core radii r_c of either $4'$, $6'$, $8'$, or $10'$. Profiles with $r_c < 4'$ are hard to distinguish from point source profiles, so for any cluster emission that is too narrow to be fit with the $r_c = 4'$ model is treated as a point source. The true spatial distribution may differ from these fiducial models, but our aim is only to extract accurate fluxes, not describe the distribution of hard X-ray emission. For Coma, a β -model fit in the first BAT band (E1: 14–20 keV) yields a total flux 9% lower than that derived from a more detailed model of its spatial distribution derived from an *XMM-Newton* temperature map (see Wik et al. 2011), which accounts for the NE-SW non-axisymmetric elongation of the emission (Eckert et al. 2007). While 9% is a significant difference, Coma is one of the most significantly detected and is the most extended cluster in the survey, so this deviation, which amounts to a factor of only 1.6 times the $1\text{-}\sigma$ error on the flux, is the

largest we would expect using this set of extended models. Also, note that no energy dependence in FWHM values is detected; e.g., Coma shows some variation with energy band, but these measurements are all consistent within their uncertainties.

We also investigated the use of diffuse models for all the clusters, irrespective of their observed extent, to account for the possibility that we are missing low surface brightness emission obscured by noise. Since the spatial distribution of $E > 10$ keV emission is unknown, we assume β -model profiles derived from ROSAT images (Reiprich & Böhringer 2002). For clusters with a clearly extended BAT profile, these models reasonably, but usually not perfectly, follow the emission; however, these profiles cannot be reliably distinguished from those at lower energies given that background fluctuations can still distort the profile due to the low signal-to-noise ratios. Spectral fits using these fluxes produce similar results to those we present in this work, but because their associated errors are larger, these spectra are generally less sensitive, so any additional flux captured — which is not significant — is also diluted. Therefore, these spectra are not considered further.

For clusters with modeled extended emission, we do not want to include the portion of flux that falls outside the *XMM-Newton* extraction region during joint fits of the data, since the complementary softer flux in the *XMM-Newton* band spectra is not present. Therefore, only the fraction of the flux that resides within the *XMM-Newton* region is included in the spectra derived here. One uncertainty, particularly when emission is detected at lower significance, is where the emission is actually coming from, given the positional accuracy of the survey (a 5σ source detected in a given band has a 90% error circle of radius $6'$). Since the E1 band-derived positions are near the center of the extraction region, within their respective error circles, we assume the center of the hard band distribution is coincident with the center of the *XMM-Newton* extraction region except for A754, A3266, and A2256. For these detected clusters, their BAT positions are somewhat offset from the surface brightness peak due to an anisotropic temperature distribution produced by mergers (see, e.g., Henry & Briel 1995; Finoguenov et al. 2006; Sun et al. 2002). Following this procedure, we will not underestimate the coincident flux, although overestimates may result that could lead to incorrect hard excesses. However, since we are unable to significantly detect non-thermal emission individually in any of the clusters, this procedure can only cause us to be biased in favor of more conservative upper limits.

3. SEPARATE FITS TO INDIVIDUAL *XMM-Newton* EPIC AND *Swift* BAT SPECTRA

Before combining the *Swift* and *XMM-Newton* datasets, we characterize each telescope’s spectra separately. The goal is to identify any problems with the data or our methodology that might lead to biased results when the spectra are fit jointly.

3.1. Single Temperature Fits to the EPIC Spectra

The motivation for including *XMM-Newton* spectra in the analysis is to fully characterize the thermal properties of the hottest gas in the ICM, which will contribute

spectra have lower signal-to-noise due to excluding the 2–3 keV emission, but the high fluxes of clusters in our sample reduce this issue’s importance. Single temperature fits in both the 2–12 keV and 3–12 keV ranges, jointly fit to all three EPIC spectra (except for A3526, for which the MOS-1 spectrum is ignored, and for A2142 and A2147, for which the MOS-2 spectra are ignored), are given in Table 2. The pn and MOS instrument cross-normalization is left as a free parameter, which allows for a typical $(10 \pm 10)\%$ difference between their calibration (e.g., Snowden 2002). This cross-normalization factor is used and kept fixed during all subsequent joint EPIC-BAT fits. The change in the best-fit temperature from the $E > 2$ keV to $E > 3$ keV fits is only ~ 0.3 keV on average, indicating that the temperature is generally robust to the choice of the energy range, but that higher energy photons come preferentially from higher temperature gas, assuming the true temperature structure is not isothermal but contains a continuous spectrum with gas at many temperatures due to substructure and/or radial gradients (Cavagnolo et al. 2008; Snowden et al. 2008).

3.2. Non-thermal Fits to the BAT Spectra

Our goal is to detect a non-thermal spectral component at hard energies, but because the statistical weight of the BAT channels is so much less than the EPIC channels (lower S/N and fewer of them, at least by an order of magnitude), we have to be careful not to let the *XMM-Newton* data unfairly drive the spectral fits. To assess the sensitivity of our BAT spectra, we extract 10,000 blank sky spectra from uniformly distributed, random positions at least $40'$ from any known sources and greater than 20° from the Galactic plane, to mimic the selection function in HIFLUGCS. We then fit these spectra with a fiducial power law model of photon index Γ fixed at a value of 2, roughly the appropriate slope for IC emission inferred from radio halos, relics, and mini-halos. While the spectral index determined from the radio is typically steeper than this (2.2–2.4), the electrons producing the radio emission at $\nu > 100$ MHz have higher energies than those producing IC at $E < 50$ keV for $B \lesssim 0.5 \mu\text{G}$, so a simple extrapolation may not be appropriate. A clear flattening of the radio spectrum at low frequencies is apparent in some cases, e.g., Coma (Thierbach et al. 2003) and A3562 (Giacintucci et al. 2005), although this is not universally found as in A2256 (Brentjens 2008) and A2255 (Pizzo & de Bruyn 2009). Since the BAT data are not particularly sensitive to the precise value of the index, we choose a flatter slope to avoid poorly fitting the data at \sim keV energies where the power law distribution of relativistic electrons is most likely to turn over in a steady state-like injection model (e.g., Sarazin 1999).

The distribution of best-fit normalizations from these power law fits are presented in the narrow histogram in Figure 2. They are well fit by a symmetric Gaussian (dashed smooth line) and indicate a 1σ sensitivity threshold of $\sim 2 \times 10^{-12} \text{ erg cm}^{-2} \text{ s}^{-1}$ (20–80 keV). Similarly, the formal 3σ detection level is $5.8 \times 10^{-12} \text{ erg cm}^{-2} \text{ s}^{-1}$. In principle, the BAT survey is sensitive enough to confirm or reject previous detections of hard excesses with fluxes $\sim 10^{-11} \text{ erg cm}^{-2} \text{ s}^{-1}$ (e.g., Rephaeli & Gruber 2002; Molendi et al. 2002; Fusco-Femiano et al. 2004).

Now we wish to compare our cluster spectra with this

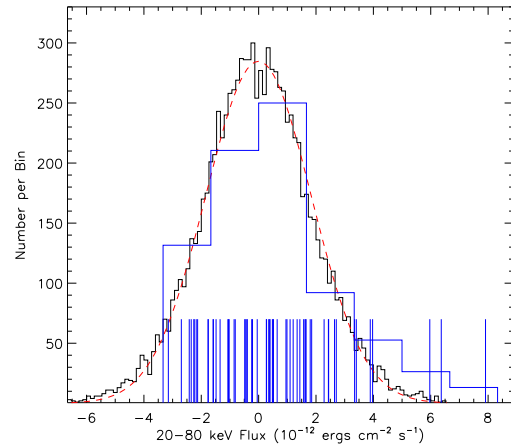


FIG. 2.— The distribution of power law normalizations (with a fixed photon index $\Gamma = 2$) fit to 10,000 blank sky spectra extracted from the BAT survey (narrowly-binned histogram). The best-fit Gaussian distribution is overlaid as the smooth, dashed line (red). Similar best-fit normalizations are shown for the 59 HIFLUGCS clusters (see text for details), with individual normalizations represented as vertical lines (blue). The cluster histogram (wide bins) has been scaled up to show its agreement with the blank sky spectra. In general, the cluster BAT spectra lack any clear evidence for a non-thermal component, except in a few cases comprising the positive tail of the blue histogram.

distribution, but first we have to account for any thermal emission in the lower energy bands. The single temperature models derived with *XMM-Newton* (2–12 keV) are included as a second component along with the power law model, with only its normalization left as a free parameter. The resulting non-thermal normalizations are also given in Figure 2 as both the wider histogram (scaled up) and as the vertical lines (showing individual values). While the majority of cluster non-thermal components are consistent with the blank sky fits, there is a tail at positive normalizations possibly indicative of a non-thermal excess. However, the thermal contribution is not well determined in this method and may be underestimated. Intriguingly, the three clusters with the most significant non-thermal component (A2029, A1367, and A1651) have positive fluxes, although marginally detected, in all 8 BAT bands; this rarely occurs for the blank sky spectra. We discuss these clusters in more detail later. The main result from this analysis is that the BAT cluster spectra have probably not reached a sensitivity level sufficient to detect hard, non-thermal excesses, if they exist, in the brightest clusters.

4. JOINT FITS TO THE EPIC-BAT SPECTRA

BAT fluxes are calibrated to match both the normalization and the spectral shape of sources as detected by the *XMM-Newton* EPIC-pn instrument (Wik et al. 2011), and they are extracted from regions identical to the *XMM-Newton* extraction regions. As such, continuous spectral models can be used over the full 2–195 keV energy range to simultaneously fit both the *XMM-Newton* and *Swift* spectra. However, in individual cases the cross-normalization factor, f_{CN} , may stray from a value of 1 as it does between the pn and MOS instruments (see Section 3.1). We therefore adopt, along with a 3% uncertainty in the *XMM-Newton* background normalizations, a conservative 10% systematic uncertainty for

TABLE 2
EPIC-ONLY, SINGLE TEMPERATURE FIT PARAMETERS

Name	Fits (2–12 keV)				Fits (3–12 keV)			
	kT (keV)	abund (Z_{\odot})	Norm. ^a (cm^{-5})	χ^2/dof	kT (keV)	abund (Z_{\odot})	Norm. ^a (cm^{-5})	χ^2/dof
A0085	6.53 ^{+0.20} _{-0.19}	0.355 ^{+0.031} _{-0.030}	0.0773 ^{+0.0012} _{-0.0012}	649.48/803	7.30 ^{+0.37} _{-0.36}	0.373 ^{+0.036} _{-0.035}	0.0728 ^{+0.0019} _{-0.0019}	395.69/525
A0119	5.73 ^{+0.48} _{-0.47}	0.227 ^{+0.069} _{-0.068}	0.0314 ^{+0.0012} _{-0.0011}	226.39/270	7.18 ^{+1.19} _{-1.03}	0.248 ^{+0.090} _{-0.084}	0.0280 ^{+0.0024} _{-0.0019}	110.39/153
A0133	3.79 ^{+0.14} _{-0.13}	0.446 ^{+0.050} _{-0.048}	0.0236 ^{+0.0006} _{-0.0006}	300.33/413	4.30 ^{+0.36} _{-0.28}	0.445 ^{+0.053} _{-0.051}	0.0207 ^{+0.0013} _{-0.0012}	129.80/228
NGC507	1.50 ^{+0.08} _{-0.08}	0.821 ^{+0.239} _{-0.189}	0.0101 ^{+0.0015} _{-0.0014}	132.82/183	1.92 ^{+0.37} _{-0.27}	0.777 ^{+0.660} _{-0.393}	0.0071 ^{+0.0025} _{-0.0018}	48.66/90
A0262	2.23 ^{+0.04} _{-0.04}	0.485 ^{+0.046} _{-0.044}	0.0549 ^{+0.0015} _{-0.0014}	584.83/668	2.37 ^{+0.10} _{-0.09}	0.395 ^{+0.056} _{-0.053}	0.0548 ^{+0.0030} _{-0.0029}	284.19/370
A0400	2.24 ^{+0.12} _{-0.12}	0.374 ^{+0.098} _{-0.098}	0.0206 ^{+0.0013} _{-0.0013}	247.76/288	2.46 ^{+0.26} _{-0.26}	0.394 ^{+0.152} _{-0.152}	0.0167 ^{+0.0026} _{-0.0026}	100.98/150
A0399	7.44 ^{+0.50} _{-0.49}	0.224 ^{+0.053} _{-0.053}	0.0356 ^{+0.0010} _{-0.0010}	269.07/368	8.10 ^{+1.17} _{-0.77}	0.237 ^{+0.062} _{-0.059}	0.0343 ^{+0.0018} _{-0.0018}	143.88/220
A3112	4.85 ^{+0.13} _{-0.13}	0.445 ^{+0.029} _{-0.029}	0.0365 ^{+0.0006} _{-0.0006}	636.64/715	5.28 ^{+0.27} _{-0.22}	0.455 ^{+0.032} _{-0.031}	0.0341 ^{+0.0012} _{-0.0012}	355.09/439
Fornax	1.66 ^{+0.03} _{-0.03}	0.743 ^{+0.070} _{-0.065}	0.0191 ^{+0.0009} _{-0.0009}	867.36/801	2.06 ^{+0.16} _{-0.14}	0.233 ^{+0.090} _{-0.080}	0.0196 ^{+0.0023} _{-0.0020}	464.04/494
2A0335	3.03 ^{+0.06} _{-0.06}	0.423 ^{+0.034} _{-0.033}	0.1014 ^{+0.0019} _{-0.0019}	482.66/649	3.22 ^{+0.13} _{-0.12}	0.395 ^{+0.036} _{-0.035}	0.0966 ^{+0.0041} _{-0.0041}	234.21/372
IIIZw54	2.63 ^{+0.11} _{-0.10}	0.297 ^{+0.058} _{-0.058}	0.0198 ^{+0.0007} _{-0.0007}	302.14/404	3.07 ^{+0.28} _{-0.24}	0.238 ^{+0.062} _{-0.062}	0.0171 ^{+0.0015} _{-0.0015}	154.89/219
A3158	5.99 ^{+0.37} _{-0.35}	0.332 ^{+0.057} _{-0.056}	0.0407 ^{+0.0012} _{-0.0012}	263.15/351	6.67 ^{+0.72} _{-0.60}	0.351 ^{+0.066} _{-0.064}	0.0376 ^{+0.0023} _{-0.0020}	146.23/208
NGC1550	1.42 ^{+0.05} _{-0.04}	0.522 ^{+0.090} _{-0.079}	0.0285 ^{+0.0023} _{-0.0022}	198.84/263	1.60 ^{+0.19} _{-0.15}	0.282 ^{+0.205} _{-0.158}	0.0292 ^{+0.0076} _{-0.0060}	78.01/119
EXO0422	3.06 ^{+0.07} _{-0.07}	0.357 ^{+0.033} _{-0.032}	0.0304 ^{+0.0006} _{-0.0006}	597.13/744	3.23 ^{+0.15} _{-0.13}	0.337 ^{+0.036} _{-0.034}	0.0284 ^{+0.0013} _{-0.0013}	318.60/437
A3266	8.34 ^{+0.30} _{-0.28}	0.196 ^{+0.030} _{-0.030}	0.0797 ^{+0.0011} _{-0.0011}	831.15/1051	8.59 ^{+0.90} _{-0.44}	0.197 ^{+0.035} _{-0.032}	0.0788 ^{+0.0021} _{-0.0021}	559.63/721
A0496	4.36 ^{+0.10} _{-0.10}	0.394 ^{+0.021} _{-0.021}	0.0835 ^{+0.0010} _{-0.0010}	1003.00/1083	4.68 ^{+0.14} _{-0.14}	0.388 ^{+0.022} _{-0.022}	0.0790 ^{+0.0019} _{-0.0019}	610.07/757
A3376	4.00 ^{+0.29} _{-0.27}	0.498 ^{+0.126} _{-0.118}	0.0108 ^{+0.0005} _{-0.0005}	129.58/167	5.76 ^{+1.15} _{-0.94}	0.454 ^{+0.146} _{-0.130}	0.0085 ^{+0.0010} _{-0.0008}	52.36/75
A3391	6.45 ^{+0.33} _{-0.31}	0.312 ^{+0.050} _{-0.049}	0.0207 ^{+0.0005} _{-0.0005}	371.79/482	6.85 ^{+0.58} _{-0.49}	0.315 ^{+0.054} _{-0.052}	0.0200 ^{+0.0009} _{-0.0008}	199.48/294
A3395s	5.76 ^{+0.66} _{-0.66}	0.248 ^{+0.102} _{-0.099}	0.0077 ^{+0.0004} _{-0.0004}	113.23/205	5.95 ^{+1.30} _{-1.13}	0.246 ^{+0.112} _{-0.104}	0.0075 ^{+0.0011} _{-0.0008}	52.46/115
R1504	8.54 ^{+0.61} _{-0.38}	0.412 ^{+0.045} _{-0.042}	0.0492 ^{+0.0011} _{-0.0011}	1629.30/1341	8.59 ^{+0.76} _{-0.51}	0.416 ^{+0.053} _{-0.047}	0.0490 ^{+0.0019} _{-0.0017}	1283.21/1010
A0576	4.06 ^{+0.28} _{-0.26}	0.377 ^{+0.083} _{-0.083}	0.0245 ^{+0.0011} _{-0.0011}	167.36/217	4.29 ^{+0.47} _{-0.47}	0.378 ^{+0.087} _{-0.087}	0.0228 ^{+0.0023} _{-0.0023}	81.90/120
A0754	9.16 ^{+0.38} _{-0.37}	0.281 ^{+0.032} _{-0.032}	0.0703 ^{+0.0008} _{-0.0008}	780.81/951	9.43 ^{+0.55} _{-0.54}	0.285 ^{+0.034} _{-0.033}	0.0697 ^{+0.0015} _{-0.0014}	523.22/636
HydraA	3.98 ^{+0.09} _{-0.09}	0.286 ^{+0.026} _{-0.025}	0.0452 ^{+0.0008} _{-0.0008}	607.64/709	4.39 ^{+0.19} _{-0.18}	0.282 ^{+0.026} _{-0.026}	0.0412 ^{+0.0015} _{-0.0014}	329.19/434
A1060	3.20 ^{+0.05} _{-0.05}	0.406 ^{+0.024} _{-0.023}	0.0592 ^{+0.0008} _{-0.0008}	853.00/963	3.44 ^{+0.10} _{-0.09}	0.384 ^{+0.024} _{-0.024}	0.0544 ^{+0.0015} _{-0.0014}	498.30/632
A1367	3.79 ^{+0.12} _{-0.12}	0.297 ^{+0.037} _{-0.036}	0.0327 ^{+0.0007} _{-0.0007}	472.97/594	4.18 ^{+0.25} _{-0.23}	0.292 ^{+0.039} _{-0.039}	0.0302 ^{+0.0016} _{-0.0014}	250.18/335
MKW4	1.69 ^{+0.11} _{-0.11}	0.660 ^{+0.190} _{-0.190}	0.0145 ^{+0.0021} _{-0.0021}	46.08/97	1.76 ^{+0.26} _{-0.26}	0.924 ^{+1.035} _{-0.535}	0.0119 ^{+0.0041} _{-0.0041}	18.41/39
ZwCl1215	7.15 ^{+0.35} _{-0.34}	0.283 ^{+0.038} _{-0.037}	0.0257 ^{+0.0005} _{-0.0005}	455.11/603	7.66 ^{+0.53} _{-0.52}	0.300 ^{+0.044} _{-0.042}	0.0248 ^{+0.0009} _{-0.0008}	269.38/363
NGC4636	0.95 ^{+0.11} _{-0.08}	0.848 ^{+0.478} _{-0.255}	0.0060 ^{+0.0016} _{-0.0015}	227.15/354	3.44 ^{+4.08} _{-1.88}	0.000 ^{+0.000} _{-0.000}	0.0019 ^{+0.0008} _{-0.0010}	95.54/145
A3526	3.95 ^{+0.04} _{-0.02}	0.544 ^{+0.010} _{-0.007}	0.1080 ^{+0.0005} _{-0.0016}	3533.06/2257	4.02 ^{+0.06} _{-0.05}	0.522 ^{+0.011} _{-0.010}	0.1085 ^{+0.0019} _{-0.0028}	2409.76/1925
A1644	5.12 ^{+0.24} _{-0.23}	0.294 ^{+0.046} _{-0.045}	0.0443 ^{+0.0012} _{-0.0012}	389.51/525	5.74 ^{+0.52} _{-0.56}	0.306 ^{+0.052} _{-0.050}	0.0412 ^{+0.0027} _{-0.0021}	227.60/296
A1650	5.96 ^{+0.17} _{-0.17}	0.393 ^{+0.026} _{-0.026}	0.0275 ^{+0.0004} _{-0.0004}	748.85/910	6.13 ^{+0.56} _{-0.25}	0.396 ^{+0.028} _{-0.028}	0.0271 ^{+0.0007} _{-0.0007}	449.63/594
A1651	6.43 ^{+0.37} _{-0.35}	0.389 ^{+0.057} _{-0.056}	0.0348 ^{+0.0011} _{-0.0011}	197.37/326	6.82 ^{+0.75} _{-0.56}	0.405 ^{+0.070} _{-0.061}	0.0338 ^{+0.0021} _{-0.0019}	118.80/190
Coma	8.53 ^{+0.19} _{-0.13}	0.248 ^{+0.015} _{-0.015}	0.2443 ^{+0.0016} _{-0.0016}	1787.94/2158	8.65 ^{+0.26} _{-0.22}	0.249 ^{+0.015} _{-0.015}	0.2439 ^{+0.0030} _{-0.0025}	1445.12/1826
NGC5044	1.21 ^{+0.04} _{-0.04}	0.797 ^{+0.148} _{-0.124}	0.0247 ^{+0.0029} _{-0.0027}	393.86/488	1.48 ^{+0.19} _{-0.14}	0.627 ^{+0.464} _{-0.294}	0.0192 ^{+0.0061} _{-0.0047}	176.46/229
A3558	5.92 ^{+0.10} _{-0.10}	0.323 ^{+0.015} _{-0.015}	0.0665 ^{+0.0005} _{-0.0005}	1271.71/1456	6.25 ^{+0.15} _{-0.15}	0.334 ^{+0.016} _{-0.016}	0.0641 ^{+0.0010} _{-0.0010}	904.58/1124
A3562	5.09 ^{+0.65} _{-0.55}	0.417 ^{+0.155} _{-0.146}	0.0175 ^{+0.0013} _{-0.0012}	54.45/125	5.69 ^{+1.13} _{-1.09}	0.416 ^{+0.028} _{-0.153}	0.0163 ^{+0.0028} _{-0.0022}	24.75/69
A3571	7.24 ^{+0.15} _{-0.15}	0.372 ^{+0.019} _{-0.019}	0.1104 ^{+0.0011} _{-0.0011}	1610.57/1874	7.57 ^{+0.21} _{-0.21}	0.385 ^{+0.021} _{-0.021}	0.1074 ^{+0.0017} _{-0.0017}	1260.22/1542
A1795	5.67 ^{+0.08} _{-0.08}	0.369 ^{+0.013} _{-0.013}	0.0797 ^{+0.0006} _{-0.0006}	1673.53/1907	5.89 ^{+0.12} _{-0.12}	0.375 ^{+0.014} _{-0.014}	0.0781 ^{+0.0011} _{-0.0011}	1337.50/1575
A3581	1.91 ^{+0.04} _{-0.04}	0.556 ^{+0.059} _{-0.055}	0.0271 ^{+0.0010} _{-0.0010}	431.36/546	2.04 ^{+0.12} _{-0.10}	0.404 ^{+0.082} _{-0.074}	0.0275 ^{+0.0024} _{-0.0023}	198.57/278
MKW8	3.36 ^{+0.30} _{-0.21}	0.350 ^{+0.099} _{-0.092}	0.0135 ^{+0.0007} _{-0.0007}	150.85/221	3.88 ^{+0.63} _{-0.48}	0.321 ^{+0.074} _{-0.097}	0.0119 ^{+0.0014} _{-0.0014}	69.64/120
A2029	7.97 ^{+0.22} _{-0.22}	0.428 ^{+0.029} _{-0.029}	0.0782 ^{+0.0010} _{-0.0010}	864.77/943	8.46 ^{+0.30} _{-0.30}	0.453 ^{+0.033} _{-0.033}	0.0754 ^{+0.0016} _{-0.0016}	539.03/632
A2052	3.01 ^{+0.05} _{-0.05}	0.500 ^{+0.029} _{-0.029}	0.0480 ^{+0.0007} _{-0.0007}	717.07/849	3.22 ^{+0.10} _{-0.09}	0.471 ^{+0.031} _{-0.031}	0.0454 ^{+0.0015} _{-0.0015}	426.04/523
MKW3S	3.36 ^{+0.06} _{-0.06}	0.388 ^{+0.027} _{-0.026}	0.0392 ^{+0.0006} _{-0.0006}	693.59/838	3.65 ^{+0.13} _{-0.12}	0.385 ^{+0.028} _{-0.028}	0.0361 ^{+0.0012} _{-0.0012}	398.37/515
A2065	6.51 ^{+0.60} _{-0.49}	0.261 ^{+0.078} _{-0.077}	0.0290 ^{+0.0018} _{-0.0018}	161.22/249	6.76 ^{+1.14} _{-0.83}	0.260 ^{+0.082} _{-0.080}	0.0282 ^{+0.0034} _{-0.0031}	95.15/156
A2063	4.34 ^{+0.14} _{-0.13}	0.345 ^{+0.034} _{-0.032}	0.0371 ^{+0.0008} _{-0.0007}	640.80/774	4.55 ^{+0.23} _{-0.22}	0.344 ^{+0.034} _{-0.033}	0.0356 ^{+0.0014} _{-0.0013}	419.72/510
A2142	9.64 ^{+2.83} _{-1.88}	0.280 ^{+0.217} _{-0.222}	0.0638 ^{+0.0051} _{-0.0051}	273.45/157	8.00 ^{+1.69} _{-1.96}	0.256 ^{+0.118} _{-0.172}	0.0678 ^{+0.0117} _{-0.0103}	131.34/93
A2147	5.17 ^{+0.58} _{-0.43}	0.238 ^{+0.100} _{-0.096}	0.0410 ^{+0.0024} _{-0.0023}	164.44/220	6.46 ^{+1.48} _{-1.06}	0.249 ^{+0.120} _{-0.113}	0.0341 ^{+0.0041} _{-0.0037}	82.91/129
A2199	4.45 ^{+0.09} _{-0.09}	0.363 ^{+0.021} _{-0.020}	0.1021 ^{+0.0012} _{-0.0012}	910.01/1069	4.59 ^{+0.14} _{-0.14}	0.366 ^{+0.022} _{-0.021}	0.0999 ^{+0.0023} _{-0.0023}	565.55/737
A2204	7.11 ^{+0.24} _{-0.23}	0.397 ^{+0.029} _{-0.028}	0.0468 ^{+0.0007} _{-0.0007}	618.61/772	7.46 ^{+0.33} _{-0.32}	0.413 ^{+0.033} _{-0.032}	0.0456 ^{+0.0012} _{-0.0012}	365.71/498
A2256	6.97 ^{+0.40} _{-0.39}	0.299 ^{+0.044} _{-0.043}	0.0530 ^{+0.0013} _{-0.0013}	324.79/434	8.07 ^{+0.67} _{-0.59}	0.338 ^{+0.056} _{-0.053}	0.0491 ^{+0.0019} _{-0.0018}	176.12/253
A2255	7.81 ^{+0.95} _{-0.87}	0.267 ^{+0.110} _{-0.107}	0.0237 ^{+0.0012} _{-0.0012}	96.21/184	8.10 ^{+1.69} _{-1.35}	0.255 ^{+0.145} _{-0.107}	0.0235 ^{+0.0023} _{-0.0020}	48.15/110
A3667	6.62 ^{+0.11} _{-0.11}	0.266 ^{+0.015} _{-0.015}	0.0761 ^{+0.0006} _{-0.0006}	1495.08/1643	7.20 ^{+0.21} _{-0.21}	0.277 ^{+0.017} _{-0.017}	0.0728 ^{+0.0010} _{-0.0010}	1141.52/1311
S1101	2.65 ^{+0.06} _{-0.06}	0.337 ^{+0.038} _{-0.037}	0.0259 ^{+0.0007} _{-0.0007}	412.70/525	2.86 ^{+0.14} _{-0.13}	0.336 ^{+0.044} _{-0.042}	0.0235 ^{+0.0013} _{-0.0013}	208.02/274
A2589	3.69 ^{+0.13} _{-0.12}	0.542 ^{+0.052} _{-0.050}	0.0205 ^{+0.0005} _{-0.00}					

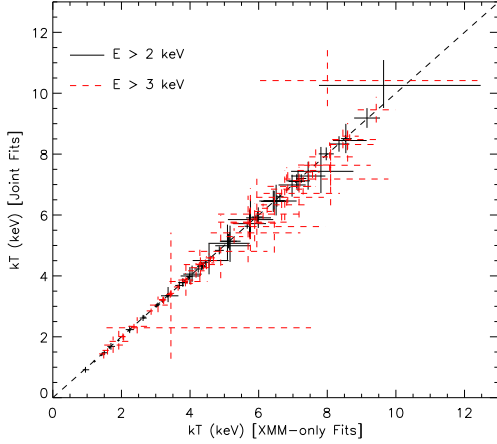


FIG. 3.— A comparison of best-fit temperature values in 1T fits to only the *XMM-Newton* spectra (x-axis) and to the EPIC and BAT spectra simultaneously (y-axis). Solid lines indicate the 90% error interval for $E > 2$ keV fits, dashed (red) lines for $E > 3$ keV, and the dashed diagonal line represents equality between the two temperature determinations. Jointly fitting both datasets yields consistent temperatures to those derived only in the *XMM-Newton* band. Fitting over a slightly higher energy range ($E > 3$ keV), while increasing the average temperature by ~ 0.3 keV in the EPIC bandpass (see text), does not increase the joint fit temperatures as much; note how the dashed points fall slightly below equality for moderately hot clusters.

f_{CN} . Because no compelling evidence for non-thermal emission is found in the nominally calibrated spectra (see analysis below), we only consider these uncertainties when deriving 90% confidence interval upper limits.

4.1. General Properties from the Joint Analysis

For each cluster, 3 simple spectral models are employed to describe the emission covering 2 orders of magnitude in energy: a single temperature thermal model (1T), a two temperature model (2T), and a thermal plus non-thermal model (T+IC). Due to the limited sensitivity of the *Swift* data, more complicated models cannot be constrained; for example, the separate temperature components in the 2T model are generally poorly constrained in our analysis. Above 50 keV, the APEC emission model is replaced with MeKa because APEC is not defined above 50 keV in the implementation of XSpec used here (Version 12.6.0k). Note that the MeKaL emission model could also be used continuously across this energy range, if the look-up table switch is turned off. For the thermal component, the temperature, abundance, redshift, and normalization are all varied. The individual abundances and redshifts in the 2T model are tied together. The non-thermal photon index is initially fixed at $\Gamma = 2$, typical of radio halos, and the normalization is allowed to vary; when the photon index is fit for, it is always fixed to the best-fit value before errors for other parameters are derived. In general, the photon index is poorly constrained, allowing for a wide range of normalizations, which are then less straightforward to evaluate. The purpose of fitting for the photon index is to make sure that we are not biased against detectable IC components with indices that differ from the fiducial value.

Because of complications arising at energies between 2 and 3 keV (see Section 3.1), we perform these fits for both the 2–195 keV (Table 5) and the 3–195 keV (Table 6)

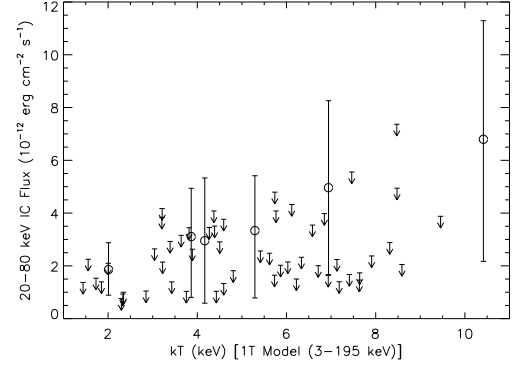


FIG. 4.— Upper limits and measurements of the non-thermal spectral component in the 3–195 keV joint fits as a function of cluster temperature. Limits and error bars indicate the 90% confidence interval without considering the impact of systematic uncertainties. In general, an excess attributable to IC emission is not observed, and the few detections, discussed individually in the text, have marginal statistical significance.

spectral ranges. The $E > 2$ keV fits, at first glance, suggest that there may be evidence for a non-thermal component in a majority of HIFLUGCS clusters. Many of the clusters with some evidence, at least at the 90% level, of a non-thermal excess are, unexpectedly, low temperature clusters without significant detections at BAT energies. In these cases, the non-thermal component is serving to “adjust” a problem at lower energies – due to either incompletely modeled low temperature components, an imperfectly calibrated response at the gold edge, or both. The significance of these instances will disappear from fits within a slightly higher energy range, while real non-thermal emission will become a higher proportion of the total flux and so this component should not greatly diminish in significance. A drastic reduction in the number of marginally detected non-thermal excesses is seen when comparing Tables 5 and 6; only 6 clusters are detected to have such emission at the 90% confidence level (statistical). These clusters will be discussed individually in Section 4.2.

While the 3–12 keV band avoids some possible systematic uncertainties with the *XMM-Newton* response and complications from cooler gas, the narrower range may reduce our ability to strongly constrain multi-temperature components in the spectra. One concern is that a weak non-thermal emission component might be indistinguishable from a purely thermal model with a slightly elevated temperature. Note, however, that the 3–12 keV band temperatures in Section 3.1 are typically only ~ 0.3 keV higher than the 2–12 keV temperatures. Therefore, the 1T model temperatures should agree for the joint fits over both energy ranges, which is found to be the case in Figure 3. Temperatures derived from joint fits are consistent with those found using only the *XMM-Newton* spectra, for both energy ranges. For the most part, temperatures from the joint fit 3–195 keV fits are in good agreement with or slightly lower than the 3–12 keV temperatures. The contribution of the BAT data in this case is to somewhat *lower* the best-fit temperature, contrary to the expectation if a detectable non-thermal excess were present. The 3–195 keV non-thermal flux limits and possible detections (90%, statistical) are shown in Figure 4.

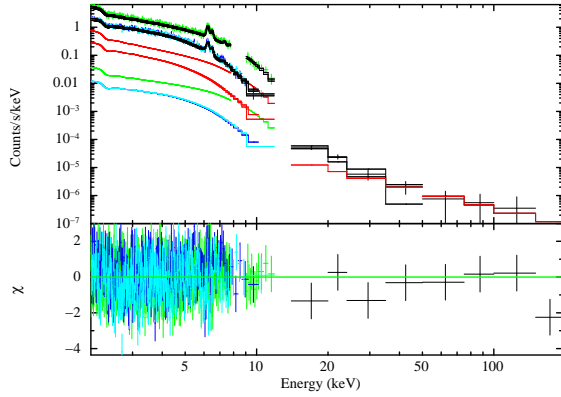


FIG. 5.— Abell 2029: The T+IC model simultaneous fit to the EPIC ($E < 12$ keV) and BAT ($E > 14$ keV, black data points and residuals) spectra. The EPIC-pn spectrum and residuals are in green, and the MOS 1 and 2 spectra/residuals are in dark and light blue, respectively. The like-colored lines below these spectra show the CXB model contribution. The total model fit and thermal contribution is represented by the black histogram, and the red lines represent the non-thermal ($\Gamma = 2$) spectral component.

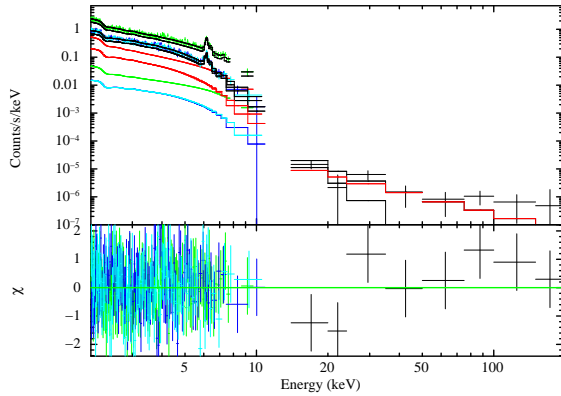


FIG. 6.— Abell 1651: The T+IC model simultaneous fit to the EPIC ($E < 12$ keV) and BAT ($E > 14$ keV) spectra. The notation is identical to Figure 5.

4.2. Individual Cases

Six clusters have a formal detection of non-thermal emission in the 3–195 keV band. Two of these 6 clusters are also in the top 3 of candidates for emission based on their BAT-only fits: A1651 and A2142. The other cluster in this top 3 – with the largest non-thermal normalization of all the clusters – is A2029, so we will include this cluster with the 6 “detected” clusters as worth some brief discussion. The clusters are listed in order of decreasing non-thermal flux.

A2029 (Fig. 5): This hot (~ 8 keV), cool core cluster has been studied in detail with *Chandra* (Clarke et al. 2004), who explore the interaction between cool gas and the radio AGN in the cluster center. The cluster is elongated but relatively regular; no evidence exists for major merger activity; however, a minor merger may be producing the spiral surface brightness enhancement in the center. Also, no evidence for an X-ray counterpart of the AGN is visible in the *Chandra* data. In addition to the radio jets, the core of the cluster is also host to an extended radio minihalo (Murgia et al. 2009). As with radio halos and relics, IC emission may be detectable from the minihalo if the magnetic field is small; Taylor et al. (1994) measured a lower limit of $B \gtrsim 0.11$ – 0.19 μ G with Fara-

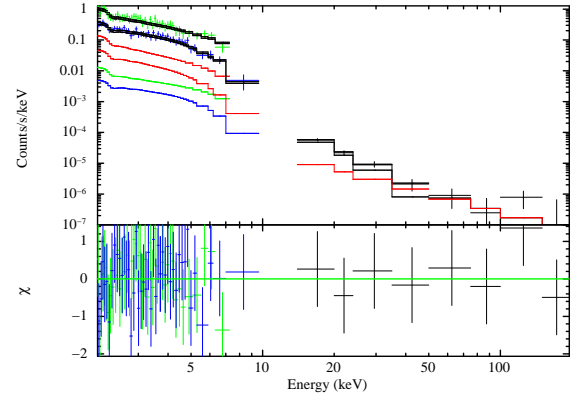


FIG. 7.— Abell 2142: The T+IC model simultaneous fit to the EPIC ($E < 12$ keV) and BAT ($E > 14$ keV) spectra. The notation is identical to Figure 5.

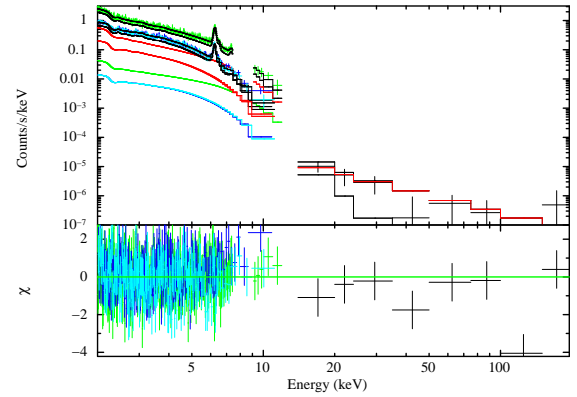


FIG. 8.— Abell 3112: The T+IC model simultaneous fit to the EPIC ($E < 12$ keV) and BAT ($E > 14$ keV) spectra. The notation is identical to Figure 5.

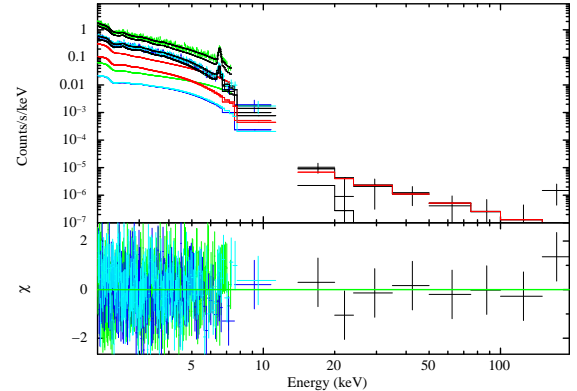


FIG. 9.— Abell 1367: The T+IC model simultaneous fit to the EPIC ($E < 12$ keV) and BAT ($E > 14$ keV) spectra. The notation is identical to Figure 5.

day RM observations of the jet. The implied magnetic field strength, if we take as the IC flux that found with the 2–195 keV fit, is $B \sim 0.08$ μ G, roughly consistent with their field strength.

But have we really detected IC from the cluster core? The significance of the non-thermal component completely disappears in the 3–195 keV fit; all three model combinations match the data equally well. Also, the 2T model formally provides a better fit to the 2–195 keV spectrum where the non-thermal component is detected.

The second temperature component, ~ 0.3 keV, is consistent with a low temperature component of 0.11 keV observed by Clarke et al. (2004). Given these results, it is more likely that the non-thermal component is trying to mimic the low kT cool core component in the 2–3 keV range, since its significance disappears if this energy range is ignored. However, it is worth noting that the BAT data do generally support hard emission at higher energies, although at low signal-to-noise. Such hard emission could be due, on the other hand, to heavily obscured emission from a background AGN within the FOV. The spatial distribution of BAT emission is consistent with that from a point source in all bands.

A1651 (Fig. 6): This cluster has a weak cool core, which means that while there is no significant temperature gradient in the center, the cooling time of the gas in the center is short (Hudson et al. 2010). Note that in a bimodal classification A1651 would not be considered to have a cool core given its high central entropy of 90 keV cm^2 (Cavagnolo et al. 2009). Given the similarity between its BAT data and that of A2029, an obscured AGN of similar flux could be responsible for the marginally detected positive flux in the higher energy bands. However, in this case the T+IC model is a significantly better fit than is the 2T model; $\Delta\chi^2$ improves by 9 (2–195 keV) and 5 (3–195 keV) over the 1T and 2T models. If there were no hard excess, the probability that the 6 highest energy bands measure flux above the thermal component, given that BAT fluctuations are Gaussian, is $(\frac{1}{2})^6$, or 1.6%, which is not impressive in a sample of 59 clusters. The BAT spectrum is certainly suggestive, but considering the excess is not significant at the 3σ level for the 3–195 keV fit, and only just at this level in the 2–195 keV fit – without including systematic uncertainties – we cannot claim to have detected a non-thermal component in this cluster. However, the evidence is perhaps strongest in this case, which is contrary to the expectation that such an excess is most likely in a merging cluster, particularly one with a radio halo or relic.

A2142 (Fig. 7): As the hottest cluster in the sample, the BAT is easily able to detect this cluster’s high energy emission, which we might expect to exhibit a non-thermal excess since it also hosts a radio halo (Giovannini & Feretti 2000). Both the T+IC and 2T models indicate that hard excess emission may be present; in the latter case, the second temperature component is unphysically high, acquiring the highest allowed temperature value. However, Nevalainen et al. (2004) estimate that 2 Seyfert galaxy nuclei within $17'$ of the cluster center contribute $\sim 30\%$ of the hard band emission detected by *Beppo-SAX*; a similar amount of contamination would be expected in the BAT spectrum. Unfortunately, the *XMM-Newton* observation places this cluster right on the edge of the FOV, so over half (55.6%, based on a comparison with a pointed *ROSAT* PSPC image) of the soft band emission is missing from the EPIC spectra. We rescale the *XMM-Newton* spectra to correct for the lost flux; the BAT source is equivalent to a point source, so it is not possible to correct the BAT emission for the *XMM-Newton* FOV. The correction to the *XMM-Newton* flux could be off by a sizable factor if the $E > 2$ keV emission is distributed differently than the

$E < 2$ keV emission where *ROSAT* is sensitive. The significance of the non-thermal excess here is only at the 2σ level, mainly due to the poor statistics at *XMM-Newton* energies. While inconclusive, the BAT spectrum warrants further analysis using better data below 12 keV.

A3112 (Fig. 8): Using both *Chandra* and *XMM-Newton* data, Bonamente et al. (2007) have claimed to see both a hard and soft excess that is consistent with a non-thermal origin. If this is the correct interpretation of these spectra, the IC excess would be clearly detectable in the BAT spectrum given our sensitivity. While a non-thermal component is detected in our joint fits, it has well below the predicted flux of Bonamente et al. (2007); our 3σ upper limit on the non-thermal normalization, using a photon index $\Gamma = 1.8$ that matches their best-fit value, is 3 times lower than their estimate. The quality of our 1T model fits is significantly less than for either the 2T or T+IC models; while those fits are of similar quality, the 2T fit yields physically reasonable temperatures and lower χ^2 values ($\Delta\chi^2 \sim 3$) than the T+IC model over both energy ranges. A non-thermal excess may in fact exist in this cluster, but a perhaps more likely scenario is that the ICM here is less isothermal than is typical in clusters, requiring several temperature components to adequately explain the cluster emission. The analysis of the *Chandra* data by Takizawa et al. (2003) in fact demonstrates the multi-temperature structure of this cluster, which may be exaggerated by significant gas cooling outside the core. In any case, the BAT data do not argue strongly in favor of an IC interpretation for the excess emission above ~ 7 keV observed in the *XMM-Newton* data; as can be seen in Figure 8, the power law component nearly ubiquitously overpredicts fluxes in the BAT spectrum. A more detailed exploration of the spatial and thermal structure at $E < 12$ keV is certainly warranted.

A1367 (Fig. 9): This cluster hosts a radio relic in its outskirts (Gavazzi & Trinchieri 1983), and so IC emission is expected at some level in the radio relic region; however, the *XMM-Newton/Swift* extraction region does not contain the relic, so we are unable to address the magnetic field strength. Using *RXTE*, Henriksen & Mushotzky (2001) potentially detect a non-thermal component, although a two temperature fit better describes their spectrum. The marginally detected IC emission we see is consistent with their non-thermal flux, whether we use a photon index of 2.0 or their value (based on the spectrum of the radio relic) of 2.9. Our 2T model fit, in the 2–195 keV band, is as good as the T+IC model fit, and given the marginally detected fluxes in the BAT bands, a 2T description of the ICM in this early stage, forming cluster cannot be ruled out. However, the positive BAT fluxes and the consistency of our non-thermal fit with the analysis of the *RXTE* spectrum warrants future investigation of this cluster’s hard X-ray emission.

A2589 & Fornax: Neither of the BAT spectra of these clusters show particular evidence that they have detected emission of any kind in any band. The first 2 bands of A2589’s spectrum are just inconsistent with zero flux at the 1σ level, but a marginal detection in these bands is consistent with the thermal component. In both cases, the BAT spectrum is not sensitive enough to exclude the non-thermal component driven by the *XMM-*

Newton data; since the BAT data do not further constrain the non-thermal component in these cases, we will not discuss these clusters further.

4.3. Upper Limits

While some evidence for non-thermal emission is present in several of the HIFLUGCS clusters, in none of these cases is a significant excess indicated by both the BAT and EPIC spectra that could not plausibly be explained by a multi-temperature state of the ICM. In many cases, the BAT spectra simply lacked the signal-to-noise to meaningfully constrain the existence of excess emission; we therefore derive upper limits for a non-thermal component in our joint spectra. Three limits are presented for each energy range (2–195 keV and 3–195 keV) considered: a 90% confidence level limit including systematic uncertainties in f_{CN} and the EPIC backgrounds, as described in Section 2.1, and two 3σ limits, without systematic uncertainties included, for our fiducial photon index of $\Gamma = 2$ and for the best-fit value of Γ . After fitting for Γ , it is then fixed at that value when the upper limit is computed. The systematic terms are included in the 90% limits as described in Wik et al. (2009). Upper limits are reported as 20–80 keV fluxes in units of $10^{-12} \text{ erg cm}^{-2} \text{ s}^{-1}$ in Table 3. Note that when Γ is much steeper than 2, the power law component is constrained only by the low energy spectrum and the 20–80 keV flux limits are not reflective of the sensitivity of the BAT survey. In some instances, usually for lower temperature clusters, the 90% limit exceeds the 3σ limits; in these fits, the systematic uncertainties in f_{CN} and/or the EPIC background dominates over the statistical uncertainty in the spectra. For example, in a low temperature cluster lowering the EPIC backgrounds significantly hardens the spectra, while modifying f_{CN} such that already poorly constraining BAT fluxes are 10% higher, will allow a much larger IC-like component to fit the data than would be allowed statistically. In hotter clusters, adjusting the background has less of an effect on their spectral shape, and because they are hot they tend to be more significantly detected by the BAT, so that modifying f_{CN} cannot drastically affect the non-thermal component.

5. JOINT FITS TO STACKED EPIC-BAT SPECTRA

In some clusters, as noted above, hints of a non-thermal excess are present, even if we cannot argue for their definite detection. If the excess does exist in several clusters, but just below the detection threshold, we may be able to increase the signal-to-noise enough for a statistical detection by stacking the cluster spectra. For simplicity, we stack only the EPIC-pn *XMM-Newton* spectra, which have the highest sensitivity especially at higher energies. Stacking the MOS spectra would be complicated by the variable pn/MOS cross-calibration factor and the fact that 3 of the cluster MOS spectra have been excluded from our analysis. Both the pn and BAT spectra are straightforwardly summed, as are the pn backgrounds, and their errors are propagated. Because the same response matrix is used for all the BAT spectra, we are able to use this unmodified file with the stacked spectrum. To create an average response matrix for use with the stacked pn spectrum, we first multiply the individual

redistribution matrices by their respective auxiliary response files, which contain the effective area per incoming photon energy. Then, a weighted average is performed on the new response files, with weighting factors proportional to each spectrum’s 2–7 keV count rate. This procedure ensures that the final response matrix will best represent the instrumental response for the majority of photons. In any case, an unweighted response file was also created and no significantly different results were produced when using it. The CXB model normalizations were summed and included in the spectral fits.

In all, we create 8 stacked spectra based on different groupings of the 59 HIFLUGCS clusters for which we have *XMM-Newton* data: “All” clusters, “Hot” ($kT > 7$ keV, from the 2–12 keV fits), “Cool” ($kT < 7$ keV), “Radio” clusters hosting either a large-scale radio halo and/or relic or a smaller, central mini-halo, “No Radio” clusters that do not host any of these types of diffuse radio emission, non-cool-core clusters (“NCC”), strong cool core clusters (“SCC”), and weak cool core clusters (“WCC”), as defined by Hudson et al. (2010) and listed in Table 1. These categories are designed to separate the sample into subgroups which might have different average levels of non-thermal emission. For example, IC emission must exist at some level in clusters with a radio halo or relic, but may not be present in clusters more generally. Thus, we might expect the “Radio” clusters to preferentially have non-thermal excesses, which are enhanced when they are stacked together and not diluted by the additional spectra from “No Radio” clusters that have no such excess.

Because these clusters span a large range of temperatures and redshifts, it is not appropriate to model the summed spectra with a single or even several temperature model for the thermal component. Instead, we build multi-temperature models from the previous spectral fits, for which we keep the spectral shape fixed and only allow the overall normalization to vary during fits to the stacked spectra. We consider the *XMM-Newton*-only single temperature fits (Table 2) derived from 2–12 keV ($1T_{\text{X},>2}$) and from 3–12 keV ($1T_{\text{X},>3}$), and the single ($1T_{\text{J}}$) and double ($2T_{\text{J}}$) temperature fits derived from the 2–195 keV joint spectra (Table 5). To search for non-thermal emission in the stacked spectra, a power law model is added to represent the IC component and the normalization of the thermal model is allowed to vary. Ideally, the shape of the thermal component would be able to adjust to accommodate the IC signal, as it effectively does in the individual joint fits via the temperature parameter. However, the non-thermal flux below 12 keV will be small and should not cause the temperature to change in any significant way. For the $2T_{\text{J}}$ model, we want to avoid including unphysical temperature components that may have been driven by calibration features at the edges of the spectral range in the individual $2T$ fits. A low temperature ($\lesssim 2$ keV) component’s emission measure may cause < 2 keV emission to be significantly overestimated in order to better fit the gold edge, for example. Similarly, a slight under-subtraction of the *XMM-Newton* background or positive fluxes in the higher energy BAT bands may lead to unrealistically high temperatures. In Figure 10, we plot the temperature values for this model relative to the $1T_{\text{J}}$ model temperatures. We have removed unphysical temperature components

TABLE 3
UPPER LIMITS TO 20–80 keV NON-THERMAL FLUX FROM EPIC AND BAT JOINT FITS

Name	Spectral Band: 2–195 keV				Spectral Band: 3–195 keV			
	90% ^a	3 $\sigma_{\Gamma=2}$ ^a	Γ	3 σ^a	90% ^a	3 $\sigma_{\Gamma=2}$ ^a	Γ	3 σ^a
A0085	0.729	6.66	2.00	6.66	0.729	6.66	1.05	5.20
A0119	1.689	6.58	2.12	6.43	1.689	6.58	9.14	3.1×10^{-7}
A0133	3.759	6.88	2.17	6.40	3.759	6.88	2.14	4.71
NGC507	1.725	1.77	1.90	2.13	1.725	1.77	1.97	2.08
A0262	0.804	4.05	2.00	4.05	0.804	4.05	3.77	0.15
A0400	0.645	2.26	9.02	2.1×10^{-8}	0.645	2.26	8.80	6.9×10^{-7}
A0399	1.818	4.04	2.07	3.62	0.032	4.04	4.53	0.01
A3112	5.420	8.98	2.00	8.98	5.420	8.98	2.18	6.98
Fornax	3.365	3.13	2.00	3.13	3.365	3.13	2.18	2.67
2A0335	1.626	6.80	2.00	6.80	1.626	6.80	2.18	4.31
III Zw54	2.626	4.32	2.14	3.48	2.626	4.32	2.33	2.63
A3158	2.453	5.08	1.93	5.24	2.453	5.08	1.98	4.56
NGC1550	2.478	1.66	2.06	1.94	2.478	1.66	2.39	1.60
EXO0422	4.171	5.18	2.01	5.14	4.171	5.18	2.03	4.98
A3266	5.131	7.25	1.98	7.43	5.131	7.25	1.89	7.87
A0496	0.733	6.28	2.00	6.28	0.733	6.28	2.11	3.33
A3376	5.582	6.01	2.10	5.03	5.582	6.01	2.02	5.77
A3391	4.609	6.30	2.00	6.25	4.609	6.30	2.00	6.08
A3395s	3.548	3.52	2.00	3.44	3.548	3.52	2.37	2.48
R1504	9.934	5.87	2.01	5.72	5.826	5.87	2.62	31.90
A0576	3.671	6.44	2.00	6.44	3.671	6.44	2.02	6.36
A0754	4.332	7.61	2.00	7.61	4.332	7.61	1.98	13.77
HydraA	4.169	8.72	2.08	8.55	4.169	8.72	2.06	5.78
A1060	0.469	7.30	2.19	7.11	0.469	7.30	2.61	1.49
A1367	5.676	8.24	2.00	8.37	5.676	8.24	2.00	7.30
MKW4	3.453	1.98	1.93	2.07	3.453	1.98	1.69	3.80
ZwCl1215	1.585	5.45	2.00	7.27	1.585	5.45	2.26	2.84
NGC4636	0.886	0.61	2.00	0.61	0.886	0.61	2.16	0.63
A3526	3.709	11.23	2.00	11.59	3.709	11.23	2.16	2.03
A1644	4.915	8.65	2.00	8.65	4.915	8.65	2.08	7.53
A1650	4.306	6.63	2.00	6.62	4.306	6.63	2.00	6.71
A1651	8.497	10.82	2.00	10.83	8.497	10.82	1.96	11.06
Coma	1.509	6.55	2.03	6.48	1.509	6.55	0.47	3.20
NGC5044	1.831	1.92	2.14	1.46	1.831	1.92	2.45	0.89
A3558	0.229	9.20	2.53	1.85	0.223	9.20	2.58	0.64
A3562	2.387	5.52	4.98	1.3×10^{-3}	2.311	5.52	8.97	7.8×10^{-7}
A3571	0.442	8.52	2.39	3.51	0.442	8.52	9.46	1.3×10^{-7}
A1795	2.143	7.22	2.68	1.09	2.143	7.22	2.10	2.99
A3581	2.351	2.76	2.00	2.75	2.351	2.76	2.34	1.70
MKW8	3.508	4.99	2.04	4.80	3.508	4.99	2.05	4.92
A2029	7.633	13.33	2.00	13.31	7.633	13.33	1.82	11.50
A2052	3.430	6.95	2.00	6.95	3.430	6.95	2.14	4.60
MKW3S	3.280	5.96	2.00	5.96	3.280	5.96	1.95	5.34
A2065	3.842	5.59	2.00	5.60	3.842	5.59	2.00	5.95
A2063	2.573	6.58	2.13	5.81	2.580	6.58	2.16	5.01
A2142	11.494	13.51	1.95	13.48	11.494	13.51	1.98	14.65
A2147	2.203	5.50	2.01	5.52	2.203	5.50	8.62	2.1×10^{-6}
A2199	3.768	7.53	2.20	8.05	3.768	7.53	2.17	5.89
A2204	5.809	11.75	2.09	9.30	5.809	11.75	2.05	8.11
A2256	3.013	7.38	2.28	5.07	3.013	7.38	2.36	2.98
A2255	1.321	2.73	6.24	2.3×10^{-5}	1.321	2.73	9.41	2.5×10^{-7}
A3667	1.932	12.00	2.39	4.01	1.932	12.00	2.20	2.79
S1101	1.009	2.23	2.43	1.65	1.009	2.23	2.08	2.13
A2589	5.045	5.82	2.00	5.82	5.045	5.82	2.02	6.42
A2597	2.620	6.10	2.00	6.09	2.620	6.10	2.41	2.90
A2634	1.806	4.34	7.28	3.3×10^{-6}	1.806	4.34	9.50	4.7×10^{-7}
A2657	0.613	4.58	2.00	4.58	0.613	4.58	7.28	2.6×10^{-5}
A4038	3.117	7.43	2.00	7.43	3.117	7.43	2.12	4.73
A4059	1.981	3.82	2.44	2.44	0.060	3.82	9.85	6.1×10^{-8}

^a 20–80 keV, 10^{-12} erg cm⁻² s⁻¹

from both the $2T_J$ model; the best-fit single temperature model is used in place of the $2T$ model for those clusters, which are represented by blue circles in Figure 10. Unphysical temperature components were found to have $kT > 16$ keV and $kT < 2.1$ keV, if their $1T_J$ temperature is greater than 3.5 keV. In general, this latter cut eliminates temperature components that significantly over-predict the $0.5 \text{ keV} < E < 2 \text{ keV}$ emission.

Thermal and thermal plus non-thermal fits to the stacked spectra are given in Table 4. Considering only the fits to data with $E > 3 \text{ keV}$, which excludes the most problematic region of the spectra, we find no evidence at the statistical 90% level for a non-thermal component in any of the stacked spectra except in the case of “Radio” clusters. In the table, the normalization of the thermal component in the “ $T_{\text{Model-only}}$ ” fits is not shown, only its χ^2 value for comparison purposes. For the “ $T_{\text{Model+IC}}$ ” fits, the photon index is fixed to $\Gamma = 2$ as was done previously for the joint fits. The last 3 columns report the “ $T_{\text{Model+IC}}$ ” fits with Γ as a free parameter; however, its value is fixed when errors are computed. In this case, the photon index was initialized as $\Gamma = 2$, so for spectra with no particularly strong indication of non-thermal emission, the best-fit normalization was set to zero and the photon index kept at or near its initialized value; this explains why so many of the “best-fit” photon indices presented in the table are ‘2.00.’ In the case of large values of $\Gamma > 3$, the non-thermal component is attempting to either represent incompletely modeled soft emission from low temperature gas or correct an imperfectly calibrated gold edge. Even though these normalizations are large and quite significant, they are so steep that the flux at hard energies is negligible and does not represent an IC excess. If $< 2 \text{ keV}$ emission were included in the fits, these large Γ values would disappear as they would vastly over-predict the soft emission.

In Figure 11, the joint fit for the stacked spectra of all 59 clusters is shown with the $1T_{X,>2}$ model. The best-fit model normalization agrees with its expected value to better than 1%, as do all the model fits without an IC component, indicating that the average pn response is accurate. Also, a difference in spectral shape appears below 3 keV, visible in the residuals, that highlights the problem with including this emission in the fits. The BAT data are well represented by this model, *even though the temperature models were derived from fits to the XMM-Newton spectra alone*. The regular pattern in the BAT residuals is likely real, and is apparent in most of the spectra of hot clusters such as Coma (see Wik et al. 2011). When considering only one cluster, it seemed reasonable that this residual pattern could simply be due to chance. The pattern reappears in many of the individual joint fits however, indicative of a systematic problem. Because the BAT flux calibration is dominated by normalizing to the Crab flux in each band, these fluxes are really only accurate for objects with a spectral slope similar to the Crab’s. At these energies, cluster spectra are quite steep even for the hottest temperatures, so some miscalibration would be expected. Most likely, the first and possibly second energy bands have underestimated fluxes, owing to the rapid rise of the instrumental response with energy; clusters have proportionately more emission at the lower energy part of the band than does the Crab, and so the internal band response is miscali-

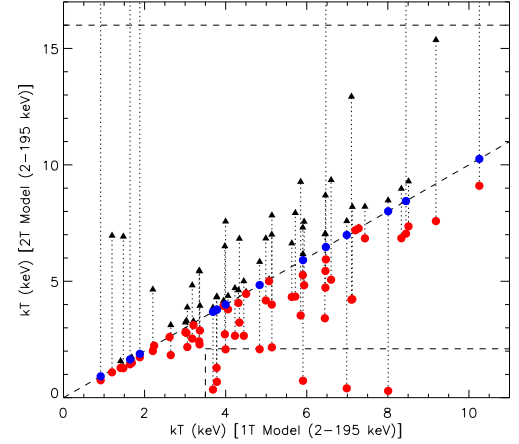


FIG. 10.— The two temperature values in the $2T$ fits (2–195 keV) with respect to the single temperature fit for each cluster over the same range. High (triangles, black) and low (circles, red) temperature values in the $2T$ model for the same cluster are connected by dotted lines for clarity. Blue circles are $1T$ fits to clusters with an unphysical best-fit $2T$ model, with either unrealistically high temperatures ($kT > 16 \text{ keV}$) or a low temperature component that over-predicts the emission below 2 keV. (These have $kT \lesssim 2.1 \text{ keV}$ for clusters with single temperatures of 3.5 keV or hotter.) These excluded regions are indicated by dashed lines in the figure, and the diagonal dashed line represents equality of $1T$ and $2T$ temperatures. These temperature values are used to build the $2T_J$ model used in fits to the stacked spectra.

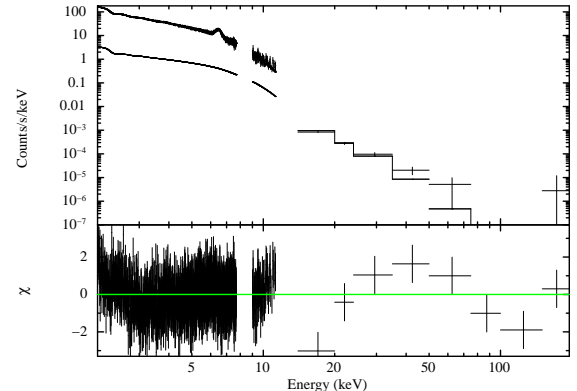


FIG. 11.— The stacked spectrum of all 59 clusters with the combined single temperature model fit ($1T_{X,>2}$). The EPIC-pn spectrum ($E < 12 \text{ keV}$) and BAT spectrum ($E > 14 \text{ keV}$) are shown in the top panel, and their residuals in the lower panel. The CXB contribution appears below the EPIC-pn data. The problems between 2–3 keV (described in the text) clearly show up in the residuals, as does a potential problem with low energy BAT fluxes. The combined single temperature model determined from the 2–12 keV fits is sufficient to explain the summed BAT spectrum; no non-thermal excess is obvious.

brated – weighting the higher energy part of the response more strongly than is appropriate for thermal emission. While this certainly affects our results, the only solution is to develop a detailed response matrix model for the survey data. Unfortunately, the detailed spectral response for the *Swift* survey data currently has much larger uncertainties than the Crab spectrum itself.

In general, the addition of a non-thermal component to these spectra does not significantly improve the fits in Table 4, *except* for the “Radio” – and to a lesser degree the “Hot” – subsamples. The “All,” “Cool,” “No Radio,” “WCC,” and “SCC” stacks are found to lack

a physically plausible ($\Gamma \lesssim 3$) non-thermal component at the statistical-only 90% level. For the “Hot” and “NCC” sample fits, the IC component improves fits using the $1T_{X,>2}$ and $1T_J$ thermal models, but not the $1T_{X,>3}$ and $2T_J$ models. In contrast, the “Radio” cluster sample $T+IC$ fits are not only clearly improved over the thermal-only fits, but the IC component is significant at the 90% level regardless of the thermal model considered. Also, except in the case of the $2T_J$ model, allowing the IC index to vary shows that the slope is consistent with expected indices (2-2.5). The exact value of the index favored by the data should not be taken to represent the true shape of the non-thermal component, however, since it is most strongly influenced by the $2 \text{ keV} < E < 3 \text{ keV}$ data and thus biased by gold edge calibration issues and incompletely modeled cool gas.

The best-fit non-thermal plus $T_{X,>2}$ model for the Radio clusters is shown in Figure 12. For comparison, the $T_{X,>2}$ and $2T_J$ fits with no IC component are shown in Figure 13 and Figure 14, respectively. The non-thermal component, plotted as a dotted line in the figure, becomes competitive with the thermal emission in the 35–50 keV band, where a somewhat significant excess is present in thermal-only model fits. By contrast, the “No Radio” subsample shows no evidence for an excess at hard energies (Fig. 15).

Ignoring systematic uncertainties, the non-thermal signature is detected for the Radio clusters with 5.1σ confidence using the $T_{X,>2}$ model and 2.4σ with the $T_{X,>3}$ model. Including a conservative f_{CN} uncertainty of 10%, which assumes the average cross-calibration is incorrect by that much, reduces the significances to 3.3σ and 0.7σ , respectively. While the detection is quite robust with the $T_{X,>2}$ thermal model, both the normalization and significance of the detection degrades when using the $T_{X,>3}$ model. Since the temperatures making up the models are not very different (see Fig. 10), the primary driver for this change must come from removing the 2–3 keV data when fitting with the $T_{X,>3}$ model. The decreased significance should not necessarily be a concern as the lowest energies statistically dominate χ^2 . However, the factor of 2 drop in flux associated with the IC component between the $T_{X,>2}+IC$ and $T_{X,>3}+IC$ fits suggests that the power law is not driven by broadband IC emission but instead by features around 2–3 keV. We cannot therefore reasonably claim an ensemble detection of excess hard emission at the 3σ level given the systematic and modeling uncertainties.

6. IMPLICATIONS AND DISCUSSION

In this work, we characterized the hard X-ray emission from HIFLUGCS, a sample of the brightest galaxy clusters outside the Galactic plane. For the 59 out of 64 clusters with usable *XMM-Newton* data, we searched for excesses over the thermal emission from gas in the ICM in data from the 58-month *Swift* BAT all-sky survey. EPIC and BAT spectra were extracted from identical regions and carefully calibrated to allow straightforward joint fits that simultaneously constrain the thermal and non-thermal emission in both spectra. We first considered fitting over an energy range of 2–195 keV but found that low temperature gas and the gold edge in the *XMM-Newton* spectra could lead to false detections. Ignoring the 2–3 keV data resolved this issue, although

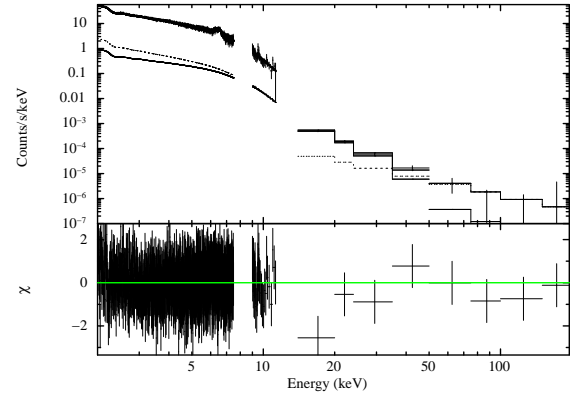


FIG. 12.— The stacked spectrum of all clusters with large-scale, diffuse radio halos or relics. General features of the plot are the same as Figure 11. The dotted line represents the best-fit non-thermal model with photon index $\Gamma = 2$, and the upper solid line shows the $1T_{X,>2}$ thermal model.

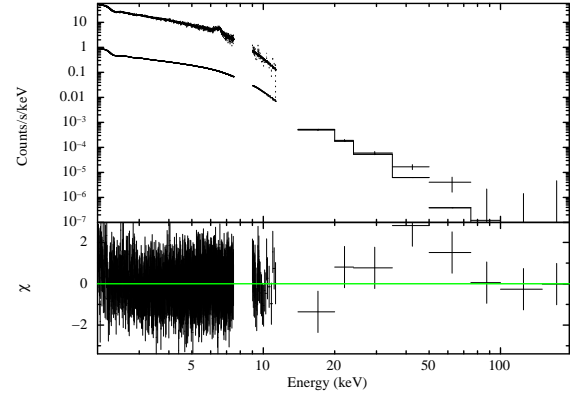


FIG. 13.— The stacked spectrum of all clusters with large-scale, diffuse radio halos or relics with the combined single temperature model fit ($1T_{X,>2}$). General features of the plot are the same as Figure 11. A slight excess is apparent in the BAT spectrum, due to either a non-thermal spectral component (see Fig. 12) or a significant multi-temperature structure in the individual clusters (see Fig. 14)

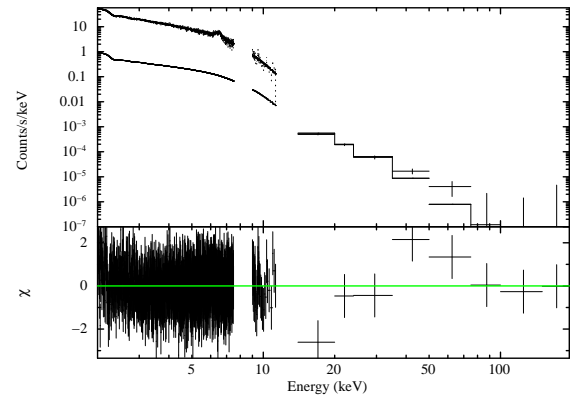


FIG. 14.— The stacked spectrum of all clusters with large-scale, diffuse radio halos or relics with the combined double temperature model fit ($2T_J$). General features of the plot are the same as Figure 11. The combined $2T_J$ model can explain most of the slight excess seen when the single temperature model ($1T_{X,>2}$) is considered.

TABLE 4
FITS TO STACKED EPIC AND BAT SPECTRA

Sample (number)	T_{Model}	$T_{\text{Model-only}}$ χ^2/dof	$T_{\text{Model+IC}}$		Γ	$T_{\text{Model+IC}}, \Gamma_{\text{free}}$	
			Norm. ^a	χ^2/dof		Norm. ^a	χ^2/dof
All (59)	$1T_{X,>2}$	1218.34/1606	< 0.0165	1217.15/1605	6.94	$1.0606^{+0.1657}_{-0.1657}$	1107.44/1605
	$1T_{X,>3}$	954.95/1406	< 0.0041	954.95/1405	2.00	< 0.0041	954.95/1405
	$1T_J$	1218.62/1606	< 0.0162	1217.56/1605	7.16	$1.2145^{+0.1926}_{-0.1926}$	1110.99/1605
	$2T_J$	1225.78/1606	< 0.0062	1225.78/1605	2.00	< 0.0062	1225.78/1605
Hot (12)	$1T_{X,>2}$	$1037.57^{+0.0049}_{-0.0049}/1606$	$0.0093^{+0.0049}_{-0.0049}$	1027.64/1605	2.21	$0.0147^{+0.0067}_{-0.0067}$	1024.50/1605
	$1T_{X,>3}$	862.44/1406	< 0.0082	861.68/1405	0.83	$< 9.3 \times 10^{-5}$	860.09/1405
	$1T_J$	1037.76/1606	$0.0088^{+0.0049}_{-0.0049}$	1028.96/1605	2.22	$0.0140^{+0.0067}_{-0.0067}$	1025.95/1605
	$2T_J$	1033.29/1606	< 0.0093	1031.20/1605	8.02	$0.5347^{+0.2086}_{-0.2086}$	1015.51/1605
Cool (47)	$1T_{X,>2}$	1101.49/1606	< 0.0069	1101.49/1605	2.00	< 0.0069	1101.49/1605
	$1T_{X,>3}$	892.09/1406	< 0.0036	892.09/1405	2.00	< 0.0036	892.09/1405
	$1T_J$	1101.51/1606	< 0.0078	1101.51/1605	7.62	$0.9748^{+0.2172}_{-0.2172}$	1047.00/1605
	$2T_J$	1098.84/1606	< 0.0034	1098.84/1605	2.00	< 0.0034	1098.84/1605
Radio (15)	$1T_{X,>2}$	1007.22/1605	$0.0137^{+0.0055}_{-0.0055}$	990.54/1604	2.29	$0.0265^{+0.0080}_{-0.0080}$	977.31/1604
	$1T_{X,>3}$	835.82/1405	$0.0061^{+0.0059}_{-0.0059}$	832.91/1404	2.01	$0.0064^{+0.0062}_{-0.0062}$	832.91/1404
	$1T_J$	1007.61/1605	$0.0130^{+0.0055}_{-0.0055}$	992.71/1604	2.32	$0.0259^{+0.0080}_{-0.0080}$	979.14/1604
	$2T_J$	1002.93/1605	$0.0079^{+0.0056}_{-0.0056}$	997.62/1604	6.80	$0.3038^{+0.0080}_{-0.0900}$	972.09/1604
No Radio (44)	$1T_{X,>2}$	1105.22/1606	< 0.0060	1105.22/1605	2.00	< 0.0060	1105.22/1605
	$1T_{X,>3}$	895.38/1406	< 0.0029	895.38/1405	2.00	< 0.0029	895.38/1405
	$1T_J$	1104.03/1606	< 0.0067	1104.03/1605	7.47	$0.8958^{+0.1910}_{-0.1910}$	1044.52/1605
	$2T_J$	1105.19/1606	< 0.0033	1105.19/1605	2.00	< 0.0033	1105.19/1605
NCC (16)	$1T_{X,>2}$	894.14/1606	$0.0054^{+0.0055}_{-0.0049}$	890.82/1605	6.67	$0.1830^{+0.0770}_{-0.0770}$	878.85/1605
	$1T_{X,>3}$	753.77/1406	< 0.0034	753.77/1405	2.00	< 0.0034	753.77/1405
	$1T_J$	892.13/1606	$0.0052^{+0.0055}_{-0.0049}$	889.10/1605	2.41	$0.0122^{+0.0076}_{-0.0076}$	885.20/1605
	$2T_J$	888.10/1606	< 0.0072	887.98/1605	7.19	$0.2277^{+0.1114}_{-0.1114}$	876.80/1605
WCC (17)	$1T_{X,>2}$	776.09/1606	< 0.0110	773.65/1605	4.18	$0.0739^{+0.0172}_{-0.0172}$	726.08/1605
	$1T_{X,>3}$	619.71/1406	< 0.0057	619.71/1405	2.00	< 0.0057	619.71/1405
	$1T_J$	775.16/1606	< 0.0104	773.29/1605	4.30	$0.0781^{+0.0185}_{-0.0185}$	726.90/1605
	$2T_J$	776.97/1606	< 0.0085	776.33/1605	4.08	$0.0681^{+0.0162}_{-0.0162}$	729.05/1605
SCC (26)	$1T_{X,>2}$	1429.48/1606	< 0.0089	1428.53/1605	9.98	$2.5281^{+0.7309}_{-0.7309}$	1397.11/1605
	$1T_{X,>3}$	1194.56/1406	< 0.0056	1194.56/1405	2.00	< 0.0056	1194.56/1405
	$1T_J$	1433.88/1606	< 0.0088	1432.82/1605	9.98	$2.6175^{+0.7326}_{-0.7326}$	1399.34/1605
	$2T_J$	1423.95/1606	< 0.0032	1423.95/1605	2.00	< 0.0032	1423.95/1605

^a At a photon energy of 1 keV in units of photons $\text{cm}^{-2} \text{s}^{-1} \text{keV}^{-1}$.

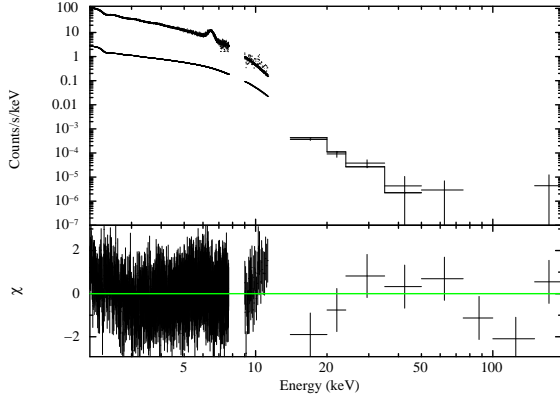


FIG. 15.— The stacked spectrum of all clusters without diffuse radio emission shown with the combined single temperature model fit ($1T_{X,>2}$). General features of the plot are the same as Figure 11.

a somewhat weaker constraint on the thermal component reduced our overall sensitivity. From the 3–195 keV fits, six clusters were found to have marginal evidence for a non-thermal excess, although none of these were deemed significant enough to claim a detection, especially considering systematic uncertainties in the EPIC background and EPIC-BAT cross calibration normaliza-

tions. We then stacked the spectra to look for a significant statistical detection of non-thermal emission in the HIFLUGCS sample. Unfortunately, the stacked spectra revealed no definitive excess. Stacking subsamples of the HIFLUGCS clusters returned similar results, except for a tantalizing but very marginal detection of a non-thermal component in the stacked spectrum of all clusters that host radio halos and/or relics or mini-halos — the very clusters that are most expected to have detectable IC emission.

6.1. Comparison to Previous Studies

The lack of definitive hard X-ray excesses in our individual clusters is consistent with the most recent searches with *Suzaku*, *INTEGRAL*, and *Swift*, though somewhat less so with those of *RXTE* and *Beppo-SAX*. Ignoring the Coma cluster, whose controversial hard energy emission is discussed at length elsewhere (e.g., Wik et al. 2011), our analysis is not clearly inconsistent with any previous observations, particularly given that the possible existence of low-level, extended non-thermal emission has not been considered in detail here (as in Wik et al. 2011), which *RXTE* and *Beppo-SAX* in particular would be sensitive to given their large FOVs. For the clusters in our sample also observed by *RXTE*, A3667 (Rephaeli & Gruber 2004) and A2256

(Rephaeli & Gruber 2003), our upper limits agree with analyses of their data, at least considering the two-temperature interpretation allowed for A2256, regardless of the distribution of emission. The recent *RXTE* detection of non-thermal emission in NGC 5044 below 15 keV by Henriksen (2011) lies below our detection threshold at higher energies. For several of the clusters observed with *Beppo-SAX* and found to host non-thermal emission, such as A2256 (Fusco-Femiano et al. 2005), A2199 (Kaastra et al. 1999), and A3526 (Molendi et al. 2002), our upper limits fall below their measured inverse Compton fluxes. Kaastra et al. (1999) claim an extended non-thermal halo for A2199 between 0.5 and 1.5 Mpc, which is not inconsistent with its larger size at high energies (14–20 keV, see Fig. 1); however, due to the low S/N of the detection, this extent is also indistinguishable from that of a point source. Upper limits from *Suzaku* for clusters A3667 (Nakazawa et al. 2009) and A3376 (Kawano et al. 2009) are obviously consistent with these results.

Similar studies of clusters detected by the BAT (Ajello et al. 2009, 2010) have also failed to find definitive non-thermal excesses. The only discrepancy is for A3667, for which both Ajello et al. (2010) and Nakazawa et al. (2009) detect high temperature ($kT \sim 15$ keV) gas near the center. While we do not see strong evidence for a significant high temperature component like this – although our 2T, 2–195 keV fit does suggest a significant amount of hot gas ($kT \sim 9$ keV) – the elongated shape caused by its ongoing merger requires a more detailed analysis to more accurately extract its BAT fluxes to properly assess this high temperature component. In any case, a noteworthy difference between the methodology here and in Wik et al. (2011) with that of Ajello et al. (2009, 2010) is our use of the technique developed by Renaud et al. (2006) to recover extended source fluxes from coded mask observations. This procedure allows for a more direct spatial comparison between soft and hard X-ray spectra such that no assumptions about the extent of hard band data need to be made; however, the low relative extent and signal-to-noise generally achieved makes this advantage critical only for the largest, brightest clusters such as Perseus and Coma.

While some excesses in the stacked spectra are tantalizing, equally good, and sometimes better, fits result when the 2T_J model is used. Since only the normalization is allowed to vary in these fits, it is hard to justify why the addition of an IC component really provides a better description of the data, especially if the improvement in χ^2 is minor. Note that this comparison is only fair because the 2T models are all physically reasonable descriptions of the ICM, otherwise we may be inappropriately modeling non-thermal emission with an incorrect thermal component. The upper limits on non-thermal emission in the stacked spectra, when applied on average to the clusters making up the stacked sample, are more constraining than limits from individual fits. The typical 90% confidence level upper limit on the cumulative IC flux in the stacked spectra is 10^{-11} erg cm⁻² s⁻¹ in the 20–80 keV band, which translates to an average maximum flux per cluster 4 to 8 times lower than this limit.

These results are in conflict with an analysis of a similar sample of clusters observed by *Beppo-SAX*

(Nevalainen et al. 2004), which found systematic if marginal excesses for merging clusters. Actually, these previous IC flux estimates are not unlike our results in the 2–195 keV range, as are the temperatures of the thermal component for clusters in both our and their samples. However, over the 3–195 keV energy range, the 90% error interval for nearly all the excesses include zero. This result is at least partly due to slightly higher best-fit temperatures (see Section 3.1 for a more detailed discussion). Since clusters are not isothermal, harder spectra such as those from the BAT will contain proportionately more photons from higher temperature gas. An example of this bias can be seen in the stacked spectrum of Nevalainen et al. (2004); they observe a highly significant non-thermal excess, but the steep IC component necessary to explain it would lead to detectable amounts of non-thermal emission at softer energies, which is not seen. The authors interpret this as evidence that the non-thermal emission is significantly extended. Our BAT data test this possibility, as extended emission is both detectable and not detected by the BAT beyond that produced by the thermal gas. Thus, it is unlikely that the non-thermal emission is very highly extended and strong. In fact, the steep excess in their spectrum is exactly what would be expected for a strongly multi-temperature thermal structure – which naturally results when many clusters spanning a broad range in temperature are summed – that is modeled as a single temperature component, which is what they do. When we model our stacked BAT spectrum this way, we find a temperature consistent with the average temperature of our clusters and a very significant, steep ($\Gamma \sim 2.8$) power law component, identical to their best-fit photon index. But the thermal component, *determined at hard energies*, will be more highly weighted by hotter clusters, whose emission dominates. If a single temperature component is used to model the thermal emission for such a summed spectrum, then at the very least the temperature needs to be fixed to the weighted-average value in the band in which the hard excess emission is expected to be found. For example, in our sample, the count rate weighted-average temperature jumps from 5.6 keV, when weighted by the 2–7 keV count rate, to 7.1 keV when the 14–50 keV count rate is used. Here we have employed the temperatures determined from the 2–12 keV fits. Even so, the exact value of the temperature is less important than the fact that the highly multi-temperature composite spectrum no longer looks like a single temperature plasma. The proper procedure is to use a truly multi-temperature model based on the temperatures of the constituent clusters, as we have done. We suspect that, if the thermal component is similarly modeled for the stacked spectrum of Nevalainen et al. (2004), the non-thermal excess will be reduced; however, it is unlikely that all of their excess would disappear.

6.2. Implied Magnetic Field Strengths

Our most suggestive result from the various stacked subsamples, that clusters hosting a radio halo or relic have the the most significant indication of a non-thermal excess on average, is also the least surprising of possible outcomes. Because radio halos and relics are associated with mergers, which also produce shocks and multi-temperature gas distributions, the more appropri-

ate thermal model to use might be the $2T_J$ model, although even in this case a non-thermal component improves the fit. Assuming the power law component represents true IC emission, we can determine the average B field in these clusters from the IC and synchrotron flux ratio as outlined in Wik et al. (2009). Unfortunately, not all of the diffuse radio emission of these clusters falls within the FOVs of the observations, so the measured IC normalization in Table 4 is not the best value we can use. We therefore sum a new subsample of cluster emission, excluding those with radio emission outside their XMM extraction regions, most notably the relics in A3667, A1367, and A3376. For the radio halo/relic clusters, we are left with radio emission from Coma (4.4 Jy at 74 MHz (Hanisch & Erickson 1980), vignetted for the extraction region), A754 (4 Jy at 74 MHz (Kassim et al. 2001)), A3562 (220 mJy at 240 MHz (Giacintucci et al. 2005)), A2256 (100 Jy at 22 MHz (Costain et al. 1972), halo and relic emission combined), A2255 (475 mJy at 150 MHz (Pizzo & de Bruyn 2009), halo emission only), and A0399 (16 mJy at 1400 MHz (Murgia et al. 2010)). Extrapolating these flux densities to a common 74 MHz given their individual spectral indices, we find a total flux of 32 Jy. Low frequency flux densities have been used where available to mitigate the effect of spectral curvature on the IC/synchrotron flux ratios. For the mini-halos, low frequency measurements are less common: A2142 (18 mJy at 1400 MHz (Giovannini & Feretti 2000)), R1504 (121 mJy at 327 MHz (Giacintucci et al. 2011)), A2029 (18.8 mJy at 1400 MHz (Murgia et al. 2009)), 2A0335 (22.6 mJy at 1500 MHz (Sarazin et al. 1995)). The two remaining mini-halos, A2204 (Sanders et al. 2009) and A2052 (Clarke, priv. comm.), do not have published diffuse fluxes. Assuming spectral indices of $\alpha = 1.3$ ($F_\nu \propto \nu^{-\alpha}$) and an average flux density of 18 mJy at 1400 MHz for all 6 clusters, a total flux of ~ 5 Jy at 74 MHz is found. Combining all these flux densities and using the power law normalization range in Table 4 (20–80 keV fluxes of $(1.3-3) \times 10^{-11}$ erg s $^{-1}$ cm $^{-2}$) yields an average $B \sim 0.13-0.19 \mu\text{G}$.

Because mini-halos are confined to the cool cores of more relaxed clusters, completely unlike large-scale halos and relics, it may be more appropriate to consider the two classes separately. Surprisingly, the fit to the new radio halo/relic stacked spectrum, made up of the clusters listed above, completely disfavors the addition of a non-thermal component. Taking the 90% statistical-only upper limit to the IC flux of 5.7×10^{-12} erg s $^{-1}$ cm $^{-2}$, we estimate $B > 0.26 \mu\text{G}$ on average in the central regions of these clusters. In contrast, the best-fit IC flux to the stacked mini-halo spectrum is 1.9×10^{-11} erg s $^{-1}$ cm $^{-2}$, significant at nearly the 4σ level (statistical-only), implying a magnetic field strength of $0.08 \mu\text{G}$ on average. For both cases the $1T_J$ thermal model is used over the 2–195 keV band. Individually, the best-fit IC fluxes of A3562, A0399, and A2255 are quite low (implying $B > 10 \mu\text{G}$) with 90% (stat.+sys.) lower limits of $0.06 \mu\text{G}$, $0.04 \mu\text{G}$, and $0.09 \mu\text{G}$, respectively. The remaining halo/relic clusters are more accommodating of a non-thermal component, with best-fit/lower limit B field strengths of $0.21/0.11 \mu\text{G}$ (A0754), $0.54/0.21 \mu\text{G}$ (Coma), and $0.46/0.33 \mu\text{G}$ (A2256). To compute

these and the following B field strengths, we use the average of the best-fit normalizations in Tables 5 and 6 and the larger upper limit from Table 3. The mini-halo spectra typically favor the additional power law component, leading to nominal best-fit IC fluxes not much lower than their upper limits and corresponding B field strengths of $0.16/0.12 \mu\text{G}$ (2A0355), $0.06/0.04 \mu\text{G}$ (A2142), $0.08/0.06 \mu\text{G}$ (A2204), $0.06/0.05 \mu\text{G}$ (A2029), $0.08/0.07 \mu\text{G}$ (A2052), and $0.10/0.05 \mu\text{G}$ (R1504), assuming a spectral index of 1.3 and radio flux densities of ~ 18 mJy at 1.4 GHz for A2052 and A2204.

These results suggest that mini-halos may involve lower B fields, more easily allowing the detection of IC emission as compared with larger halos and relics. This general conclusion is consistent with the measurement of non-thermal emission with *INTEGRAL* associated with the mini-halo in the core of the Ophiuchus cluster that implies $B = 0.05-0.1 \mu\text{G}$ (Nevalainen et al. 2009). While it is tempting to associate the IC flux with the entire mini-halo sample, the vast majority of the BAT flux originates with A2029 and A2142 (three-quarters of the 14–24 keV emission and $> 90\%$ of it at the higher energies). These two cases are discussed individually in Section 4.2. A2142 is particularly problematic, in that the *XMM-Newton* extraction region only contains half the cluster, which adds significant systematic uncertainty to the cross-calibration with the BAT spectrum, and in that the classification of the diffuse radio emission as a mini-halo, as opposed to radio galaxy jets, is not ironclad. We are therefore precluded from drawing strong conclusions from this result, which is robustly driven by only a single cluster: A2029. In any case, the non-thermal component in the mini-halo spectrum is consistent with and somewhat driven by the BAT measurements, suggesting that mini-halos may be better targets of future hard X-ray observations, especially given their smaller size, than traditional halos and relics.

It may not be surprising that IC emission was not detected definitively in the radio halo/relic clusters; direct measurements of cluster magnetic fields through Faraday rotation measure (RM) studies typically find line-of-sight B fields on the order of several μG (Govoni & Feretti 2004). Similar high values of B are suggested by the stability of cold fronts in merging clusters (Keshet et al. 2010), although the flow may locally amplify the fields in these regions, so they would not be representative of the global average field strength, even in mini-halos. Also, RM magnetic field strengths could be biased high if stronger fields are correlated with denser gas, since RM observations are really measuring the electron density-weighted value of B along the line of sight (Petrosian 2001). Such explanations, while entirely reasonable, were primarily developed to explain the lower values of B implied by earlier IC detections, some of which have been more recently called into question (e.g., with *Suzaku*, Nakazawa et al. 2007, 2009; Wik et al. 2009). However, if our low significance evidence for IC emission associated with mini-halos can be corroborated, then such low values of B may in fact be common. Our current sensitivity to IC emission with either pointed or survey observations can only detect non-thermal emission in clusters with radio halos if the magnetic fields are $\lesssim 0.2 \mu\text{G}$. Note that it is possible to observe much fainter IC emission at lower X-ray energies, and thus measure larger B fields, in ra-

dio relics that are significantly displaced from the X-ray luminous gas in cluster centers (Finoguenov et al. 2010).

6.3. Dynamical Importance of the Non-thermal Electron Population

Given that we have searched for and provided limits on IC emission from relativistic electron populations in a complete sample of clusters, what does that tell us about the general energetic importance of this population relative to the thermal electron population of clusters in the low redshift universe? Hydrostatic cluster mass estimates – employed by studies using clusters as cosmological probes – typically assume a negligible amount of non-thermal pressure in central regions. In the following, we attempt to confirm this presumption. A power law IC spectrum is thought to originate from an energy distribution of relativistic electrons proportional to γ^{-p} , where γ is the electron Lorentz factor and $p = 2\alpha + 1 = 2\Gamma - 1$. The total energy in these electrons depends on the range of γ s and is particularly sensitive to the lower cut off energy where most of the electrons reside. Following Murgia et al. (2010), a rare case in which rough observational estimates exist, we take $\gamma_{\min} \sim 300$ and $\gamma_{\max} \sim 3 \times 10^4$. The large uncertainty in these choices, which are impossible for us to estimate since 2–200 keV energies correspond to $1500 \lesssim \gamma \lesssim 1.5 \times 10^4$, limits the following discussion to order of magnitude estimates at best.

Our goal is to compare the typical non-thermal pressure, $P_{\text{NT}} = u_{\text{NT}}/3$, where u_{NT} is the energy density of the non-thermal population, to the typical thermal pressure inside our extraction regions. For simplicity, we adopt the universal pressure profile of Arnaud et al. (2010) from which the thermal pressure inside the region (taken to be $\sim \frac{2}{3}$ of the extraction radius) can be derived from the mass estimates at R_{500} of Zhang et al. (2011). In individual clusters, the 90% upper limits on the IC flux typically limit the non-thermal electron to thermal electron pressure to less than a few tens of percent. The limits are stricter for massive (hot) clusters ($\lesssim 10\%$), primarily because the IC limits are all roughly comparable as a result of the uniformity of the BAT sensitivity. If we instead take the best-fit IC normalizations, the non-thermal pressure of nearly all of the clusters is less than 10% of thermal pressure with massive clusters typically at less than a few percent. Except for the least massive clusters in HIFLUGCS, the comparable magnetic field pressure assuming $B = 1\mu\text{G}$ corresponds to $\sim 1\%$ of the thermal pressure. Although we cannot measure B fields this large in the radio clusters, as long as $B \lesssim 3\text{--}7\mu\text{G}$, it seems unlikely that non-thermal pressure support will significantly contribute in cluster centers, especially for the more massive clusters that are typically used for cosmological parameter estimation.

6.4. Future Outlook

Can the survey observations with the BAT be improved, beyond the increase in sensitivity which comes with longer accumulating exposures? Perhaps the clearest way forward is to better calibrate the spectral response of the BAT in narrower channel so that the fluxes are more reliable for steep thermal emission in the 14–24 keV energy range. At present, we may be underestimating source fluxes in these bands. If the first band is low by $\sim 2\sigma$ and the second by $\sim 1\sigma$, as suggested by the residuals in Figure 11, our non-thermal limits will increase by about 1σ – a small but non-negligible amount. The most straightforward fix is to remake the survey using the BAT’s native 80 channels instead of binning them into 8 channels that are broad enough to be biased by the flux calibration with the Crab. With such improved data, this study can be repeated with a sample of all the known radio halo and relic clusters to definitively detect the non-thermal excess hinted at in the stacked “Radio” subsample considered here, if it exists.

Ultimately, any IC detections, especially if marginal, will have to be confirmed by the upcoming missions with focussing hard X-ray telescopes, namely *NuSTAR*⁸ and *Astro-H*⁹. By resolving both contaminating point sources and the location of the hottest gas, these missions have the potential to achieve higher sensitivities than have thus far been possible. Also, these telescopes’ narrow FOVs are well-suited to the smaller angular extents of mini-halos, making them ideal targets even though the radio flux densities are typically lower.

We particularly owe the *Swift* BAT team a hearty thanks for uniformly processing the tens of thousands of individual pointings that make up the BAT survey that allow it to be such an incredibly useful resource for studies like ours. DRW and CLS were supported in part by NASA through Suzaku grants NNX08AZ99G, NNX09AH25G, and NNX09AH74G, and XMM-Newton grants NNX08AZ34G and NNX08AW83G. YYZ acknowledges support from the German BMBF through the Verbundforschung under grant No. 50 OR 1005. The XMM-Newton project is an ESA Science Mission with instruments and contributions directly funded by ESA Member States and the USA (NASA), and it is supported by the Bundesministerium für Wirtschaft und Technologie/Deutsches Zentrum für Luft- und Raumfahrt (BMWi/DLR, FKZ 50 OX 0001) and the Max-Planck Society. Basic research in radio astronomy at the Naval Research Laboratory is supported by 6.1 Base funding. This research was also supported in part by an appointment to the NASA Postdoctoral Program at the Goddard Space Flight Center, administered by Oak Ridge Associated Universities through a contract with NASA.

REFERENCES

- Ajello, M., et al. 2009, ApJ, 690, 367
 Ajello, M., Rebusco, P., Cappelluti, N., Reimer, O., Böhringer, H., La Parola, V., & Cusumano, G. 2010, ApJ, 725, 1688
 Arnaud, M., Pratt, G. W., Piffaretti, R., et al. 2010, A&A, 517, A92
 Bonamente, M., Nevalainen, J., & Lieu, R. 2007, ApJ, 668, 796
 Bonamente, M., Lieu, R., & Bulbul, E. 2009, ApJ, 696, 1886
 Brentjens, M. A. 2008, A&A, 489, 69
 Brunetti, G., & Blasi, P. 2005, MNRAS, 363, 1173
 Buote, D. A. 2001, ApJ, 553, L15
 Cavagnolo, K. W., Donahue, M., Voit, G. M., & Sun, M. 2008, ApJ, 682, 821
⁸ <http://www.nustar.caltech.edu/>
⁹ <http://astro-h.isas.jaxa.jp/>

- Cavagnolo, K. W., Donahue, M., Voit, G. M., & Sun, M. 2009, *ApJS*, 182, 12
- Clarke, T. E., Blanton, E. L., & Sarazin, C. L. 2004, *ApJ*, 616, 178
- Costain, C. H., Bridle, A. H., & Feldman, P. A. 1972, *ApJ*, 175, L15
- De Luca, A., & Molendi, S. 2004, *A&A*, 419, 837
- Eckert, D., Neronov, A., Courvoisier, T. J.-L., & Produit, N. 2007, *A&A*, 470, 835
- Eckert, D., Produit, N., Paltani, S., Neronov, A., & Courvoisier, T. J.-L. 2008, *A&A*, 479, 27
- Eckert, D., Molendi, S., & Paltani, S. 2011, *A&A*, 526, A79
- Finoguenov, A., Henriksen, M. J., Miniati, F., Briel, U. G., & Jones, C. 2006, *ApJ*, 643, 790
- Finoguenov, A., Sarazin, C. L., Nakazawa, K., Wik, D. R., & Clarke, T. E. 2010, *ApJ*, 715, 1143
- Fusco-Femiano, R., Orlandini, M., Brunetti, G., Feretti, L., Giovannini, G., Grandi, P., & Setti, G. 2004, *ApJ*, 602, L73
- Fusco-Femiano, R., Landi, R., & Orlandini, M. 2005, *ApJ*, 624, L69
- Gavazzi, G., & Trinchieri, G. 1983, *ApJ*, 270, 410
- Giaccintucci, S., Venturi, T., Brunetti, G., et al. 2005, *A&A*, 440, 867
- Giaccintucci, S., Markevitch, M., Brunetti, G., Cassano, R., & Venturi, T. 2011, *A&A*, 525, L10
- Giovannini, G., & Feretti, L. 2000, *New Astron.*, 5, 335
- Govoni, F., & Feretti, L. 2004, *International Journal of Modern Physics D*, 13, 1549
- Hanisch, R. J., & Erickson, W. C. 1980, *AJ*, 85, 183
- Henriksen, M., & Mushotzky, R. 2001, *ApJ*, 553, 84
- Henriksen, M. J. 2011, *ApJ*, 726, 9
- Henry, J. P., & Briel, U. G. 1995, *ApJ*, 443, L9
- Hudson, D. S., Mittal, R., Reiprich, T. H., Nulsen, P. E. J., & Andernach, H., & Sarazin, C. L. 2010, *A&A*, 513, A37
- Kaastra, J. S., Lieu, R., Mittal, J. P. D., Bleeker, J. A. M., Mewe, R., Colafrancesco, S., & Lockman, F. J. 1999, *ApJ*, 519, L119
- Kassim, N. E., Clarke, T. E., Enßlin, T. A., Cohen, A. S., & Neumann, D. M. 2001, *ApJ*, 559, 785
- Kawano, N., et al. 2009, *PASJ*, 61, 377
- Kempner, J. C., & Sarazin, C. L. 2000, *ApJ*, 530, 282
- Keshet, U., Markevitch, M., Birnboim, Y., & Loeb, A. 2010, *ApJ*, 719, L74
- Koutroumpa, D., Lallement, R., Kharchenko, V., & Dalgarno, A. 2009, *Space Sci. Rev.*, 143, 217
- Lumb, D. H., Warwick, R. S., Page, M., & De Luca, A. 2002, *A&A*, 389, 93
- Mantz, A., Allen, S. W., Ebeling, H., & Rapetti, D. 2008, *MNRAS*, 387, 1179
- Molendi, S., De Grandi, S., & Guainazzi, M. 2002, *A&A*, 392, 13
- Moretti, A., Campana, S., Lazzati, D., & Tagliaferri, G. 2003, *ApJ*, 588, 696
- Murgia, M., Govoni, F., Markevitch, M., Feretti, L., Giovannini, G., Taylor, G. B., & Carretti, E. 2009, *A&A*, 499, 679
- Murgia, M., Eckert, D., Govoni, F., et al. 2010, *A&A*, 514, A76
- Murgia, M., Govoni, F., Feretti, L., & Giovannini, G. 2010, *A&A*, 509, A86
- Nakazawa, K., et al. 2007, *Progress of Theoretical Physics Supplement*, 169, 45
- Nakazawa, K., et al. 2009, *PASJ*, 61, 339
- Nevalainen, J., Oosterbroek, T., Bonamente, M., & Colafrancesco, S. 2004, *ApJ*, 608, 166
- Nevalainen, J., Eckert, D., Kaastra, J., Bonamente, M., & Kettula, K. 2009, *A&A*, 508, 1161
- Petrosian, V. 2001, *ApJ*, 557, 560
- Pizzo, R. F., & de Bruyn, A. G. 2009, *A&A*, 507, 639
- Reiprich, T. H., & Böhringer, H. 2002, *ApJ*, 567, 716
- Renaud, M., Gros, A., Lebrun, F., Terrier, R., Goldwurm, A., Reynolds, S., & Kalemci, E. 2006, *A&A*, 456, 389
- Rephaeli, Y. 1979, *ApJ*, 227, 364
- Rephaeli, Y., Gruber, D., & Arieli, Y. 2006, *ApJ*, 649, 673
- Rephaeli, Y., & Gruber, D. 2002, *ApJ*, 579, 587
- Rephaeli, Y., & Gruber, D. 2003, *ApJ*, 595, 137
- Rephaeli, Y., & Gruber, D. 2004, *ApJ*, 606, 825
- Rossetti, M., & Molendi, S. 2004, *A&A*, 414, L41
- Sanders, J. S., Fabian, A. C., & Taylor, G. B. 2009, *MNRAS*, 393, 71
- Sarazin, C. L. 1999, *ApJ*, 520, 529
- Sarazin, C. L., Baum, S. A., & O'Dea, C. P. 1995, *ApJ*, 451, 125
- Schuecker, P., Böhringer, H., Reiprich, T. H., & Feretti, L. 2001, *A&A*, 378, 408
- Snowden, S. L. 2002, *arXiv:astro-ph/0203311*
- Snowden, S. L., Mushotzky, R. F., Kuntz, K. D., & Davis, D. S. 2008, *A&A*, 478, 615
- Sun, M., Murray, S. S., Markevitch, M., & Vikhlinin, A. 2002, *ApJ*, 565, 867
- Takei, Y., Henry, J. P., Finoguenov, A., Mitsuda, K., Tamura, T., Fujimoto, R., & Briel, U. G. 2007, *ApJ*, 655, 831
- Takizawa, M., Sarazin, C. L., Blanton, E. L., & Taylor, G. B. 2003, *ApJ*, 595, 142
- Taylor, G. B., Barton, E. J., & Ge, J. 1994, *AJ*, 107, 1942
- Thierbach, M., Klein, U., & Wielebinski, R. 2003, *A&A*, 397, 53
- Tueller, J., et al. 2010, *ApJS*, 186, 378
- Wik, D. R., Sarazin, C. L., Finoguenov, A., Matsushita, K., Nakazawa, K., & Clarke, T. E. 2009, *ApJ*, 696, 1700
- Wik, D. R., Sarazin, C. L., Finoguenov, A., Baumgartner, W. H., Mushotzky, R. F., Okajima, T., Tueller, J., & Clarke, T. E. 2011, *ApJ*, 727, 119
- Wilson-Hodge, C. A., et al. 2011, *ApJ*, 727, L40
- Winter, L. M., Mushotzky, R. F., Reynolds, C. S., & Tueller, J. 2009, *ApJ*, 690, 1322
- Vanderlinde, K., et al. 2010, *arXiv:1003.0003*
- Vikhlinin, A., et al. 2009, *ApJ*, 692, 1060
- Zhang, Y.-Y., Reiprich, T. H., Finoguenov, A., Hudson, D. S., & Sarazin, C. L. 2009, *ApJ*, 699, 1178
- Zhang, Y.-Y., Andernach, H., Caretta, C. A., Reiprich, T. H., Böhringer, H., Puchwein, E., Sijacki, D., & Girardi, M. 2011, *A&A*, 526, A105

TABLE 5
JOINT THERMAL AND NON-THERMAL FITS TO THE EPIC AND BAT SPECTRA
(2–195 keV)

Name	Model ^a	Component 1			Component 2		χ^2/dof
		kT (keV)	abund Z_{\odot}	Norm. ^b (cm^{-5})	kT (keV)	Norm. ^c	
A0085	1T	$6.46^{+0.19}_{-0.18}$	$0.358^{+0.031}_{-0.030}$	$0.0775^{+0.0010}_{-0.0010}$	8.69	0.0283	654.76/812
	2T	5.44	0.368	0.0497			653.27/810
A0119	T+IC	$6.46^{+0.19}_{-0.19}$	$0.365^{+0.036}_{-0.035}$	$0.0760^{+0.0025}_{-0.0042}$	7.94	< 0.0019	654.35/811
	1T	$5.72^{+0.46}_{-0.45}$	$0.223^{+0.069}_{-0.068}$	$0.0316^{+0.0011}_{-0.0010}$			231.53/279
A0133	2T	4.34	0.240	0.0183	4.34	0.0138	229.46/277
	T+IC	$5.66^{+0.49}_{-0.48}$	$0.243^{+0.078}_{-0.076}$	$0.0295^{+0.0029}_{-0.0040}$			230.33/278
NGC507	1T	$3.78^{+0.14}_{-0.13}$	$0.446^{+0.050}_{-0.048}$	$0.0236^{+0.0006}_{-0.0006}$	6.92	0.0206	302.63/422
	2T	0.68	0.452	0.0133		0.0018 ^{+0.0007} _{-0.0014}	285.74/420
A0262	T+IC	$3.36^{+0.40}_{-0.20}$	$0.640^{+0.147}_{-0.178}$	$0.0175^{+0.0047}_{-0.0024}$			297.02/421
	1T	$1.48^{+0.08}_{-0.08}$	$0.827^{+0.248}_{-0.193}$	$0.0100^{+0.0015}_{-0.0014}$	4.65	0.0004 ^{+0.0002} _{-0.0002}	144.17/192
A0400	2T	1.27	0.876	0.0095		0.0008	136.45/190
	T+IC	$1.28^{+0.14}_{-0.12}$	$0.990^{+0.474}_{-0.275}$	$0.0084^{+0.0020}_{-0.0021}$			137.27/191
A0400	1T	$2.20^{+0.04}_{-0.04}$	$0.485^{+0.046}_{-0.044}$	$0.0545^{+0.0014}_{-0.0014}$	4.65	0.0052	591.81/677
	2T	2.00	0.482	0.0508		0.0008 ^{+0.0006} _{-0.0007}	588.00/675
A0400	T+IC	$2.12^{+0.09}_{-0.06}$	$0.520^{+0.057}_{-0.052}$	$0.0519^{+0.0025}_{-0.0025}$			588.14/676
	1T	$2.24^{+0.12}_{-0.11}$	$0.368^{+0.108}_{-0.098}$	$0.0207^{+0.0014}_{-0.0013}$			265.48/297

TABLE 5 — *Continued*

Name	Model ^a	Component 1			Component 2		χ^2/dof
		kT (keV)	abund Z_{\odot}	Norm. ^b (cm^{-5})	kT (keV)	Norm. ^c	
A0399	2T	2.23	0.366	0.0095	2.24	0.0112	265.30/295
	T+IC	$2.23^{+0.13}_{-0.13}$	$0.359^{+0.115}_{-0.091}$	$0.0208^{+0.0013}_{-0.0020}$		< 0.0005	265.30/296
	1T	$7.28^{+0.47}_{-0.45}$	$0.224^{+0.052}_{-0.052}$	$0.0357^{+0.0007}_{-0.0007}$			276.34/377
	2T	7.30	0.224	0.0108	7.27	0.0249	276.34/375
A3112	T+IC	$7.29^{+0.46}_{-0.45}$	$0.223^{+0.053}_{-0.051}$	$0.0357^{+0.0007}_{-0.0027}$		< 0.0009	276.34/376
	1T	$4.84^{+0.13}_{-0.13}$	$0.447^{+0.030}_{-0.029}$	$0.0365^{+0.0006}_{-0.0005}$			655.48/724
	2T	2.08	0.495	0.0097	5.84	0.0284	635.35/722
Fornax	T+IC	$4.64^{+0.19}_{-0.17}$	$0.567^{+0.066}_{-0.076}$	$0.0284^{+0.0037}_{-0.0026}$		$0.0025^{+0.0008}_{-0.0011}$	638.12/723
	1T	$1.64^{+0.03}_{-0.03}$	$0.748^{+0.071}_{-0.066}$	$0.0188^{+0.0009}_{-0.0009}$			847.93/810
	2T	1.43	0.796	0.0175	20.57	0.0016	777.35/808
2A0335	T+IC	$1.41^{+0.05}_{-0.05}$	$1.038^{+0.163}_{-0.133}$	$0.0134^{+0.0014}_{-0.0014}$		$0.0011^{+0.0002}_{-0.0002}$	759.76/809
	1T	$3.03^{+0.06}_{-0.06}$	$0.424^{+0.034}_{-0.033}$	$0.0999^{+0.0017}_{-0.0017}$			506.39/658
	2T	2.78	0.424	0.0524	3.31	0.0475	506.39/656
IIIZw54	T+IC	$2.99^{+0.09}_{-0.09}$	$0.438^{+0.044}_{-0.042}$	$0.0976^{+0.0037}_{-0.0043}$		< 0.0019	505.54/657
	1T	$2.62^{+0.10}_{-0.09}$	$0.299^{+0.062}_{-0.059}$	$0.0198^{+0.0008}_{-0.0007}$			303.72/413
	2T	2.61	0.299	0.0103	2.63	0.0095	303.73/411
A3158	T+IC	$2.20^{+0.31}_{-0.17}$	$0.407^{+0.092}_{-0.114}$	$0.0160^{+0.0028}_{-0.0014}$		$0.0012^{+0.0004}_{-0.0008}$	298.06/412
	1T	$5.91^{+0.35}_{-0.33}$	$0.333^{+0.057}_{-0.056}$	$0.0407^{+0.0010}_{-0.0010}$			268.83/360
	2T	0.73	0.346	0.0066	6.17	0.0393	267.43/358
NGC1550	T+IC	$5.85^{+0.35}_{-0.35}$	$0.343^{+0.065}_{-0.062}$	$0.0395^{+0.0020}_{-0.0034}$		< 0.0014	270.38/359
	1T	$1.41^{+0.05}_{-0.04}$	$0.519^{+0.090}_{-0.079}$	$0.0286^{+0.0023}_{-0.0022}$			199.27/272
	2T	1.28	0.532	0.0172	1.57	0.0116	198.50/270
EXO0422	T+IC	$1.31^{+0.08}_{-0.08}$	$0.552^{+0.107}_{-0.089}$	$0.0274^{+0.0029}_{-0.0027}$		$0.0005^{+0.0003}_{-0.0003}$	192.68/271
	1T	$3.05^{+0.07}_{-0.07}$	$0.359^{+0.033}_{-0.032}$	$0.0303^{+0.0005}_{-0.0005}$			604.98/753
	2T	2.18	0.363	0.0148	3.88	0.0164	600.49/751
A3266	T+IC	$2.78^{+0.20}_{-0.14}$	$0.457^{+0.041}_{-0.062}$	$0.0258^{+0.0031}_{-0.0021}$		$0.0013^{+0.0006}_{-0.0009}$	598.20/752
	1T	$8.33^{+0.26}_{-0.25}$	$0.193^{+0.030}_{-0.030}$	$0.0797^{+0.0009}_{-0.0009}$			836.80/1060
	2T	6.85	0.194	0.0203	8.98	0.0595	835.89/1058
A0496	T+IC	$8.35^{+0.27}_{-0.26}$	$0.206^{+0.032}_{-0.031}$	$0.0761^{+0.0018}_{-0.0035}$		$0.0012^{+0.0011}_{-0.0012}$	833.17/1059
	1T	$4.34^{+0.08}_{-0.10}$	$0.397^{+0.023}_{-0.021}$	$0.0835^{+0.0011}_{-0.0008}$			1011.89/1092
	2T	3.23	0.451	0.0556	6.83	0.0302	999.75/1090
A3376	T+IC	$4.28^{+0.13}_{-0.08}$	$0.414^{+0.025}_{-0.033}$	$0.0810^{+0.0034}_{-0.0032}$		< 0.0019	1011.04/1091
	1T	$4.00^{+0.29}_{-0.27}$	$0.499^{+0.126}_{-0.118}$	$0.0108^{+0.0005}_{-0.0005}$			140.99/176
	2T	2.08	0.579	0.0061	7.57	0.0054	130.29/174
A3391	T+IC	$3.06^{+0.59}_{-0.46}$	$1.329^{+1.706}_{-0.586}$	$0.0045^{+0.0026}_{-0.0024}$		$0.0018^{+0.0005}_{-0.0008}$	130.39/175
	1T	$6.47^{+0.32}_{-0.31}$	$0.311^{+0.050}_{-0.049}$	$0.0207^{+0.0004}_{-0.0004}$			375.51/491
	2T	5.94	0.321	0.0195	47.56	0.0016	372.46/489
A3395s	T+IC	$6.56^{+0.39}_{-0.38}$	$0.379^{+0.064}_{-0.087}$	$0.0168^{+0.0034}_{-0.0023}$		$0.0012^{+0.0008}_{-0.0011}$	371.91/490
	1T	$5.85^{+0.66}_{-0.64}$	$0.228^{+0.095}_{-0.093}$	$0.0078^{+0.0004}_{-0.0003}$			118.38/214
	2T	3.53	0.306	0.0041	9.27	0.0039	114.33/212
R1504	T+IC	$5.79^{+0.75}_{-0.74}$	$0.282^{+0.163}_{-0.114}$	$0.0067^{+0.0014}_{-0.0020}$		< 0.0009	117.05/213
	1T	$8.45^{+0.55}_{-0.41}$	$0.416^{+0.049}_{-0.047}$	$0.0491^{+0.0011}_{-0.0010}$			1187.05/1053
	2T	7.05	0.425	0.0364	17.30	0.0135	1183.65/1051
A0576	T+IC	$11.47^{+1.32}_{-0.92}$	$0.453^{+0.143}_{-0.105}$	$0.0437^{+0.0058}_{-0.0058}$		$0.0016^{+0.0015}_{-0.0015}$	1272.90/1052
	1T	$4.06^{+0.28}_{-0.26}$	$0.376^{+0.087}_{-0.083}$	$0.0244^{+0.0010}_{-0.0010}$			175.63/226
	2T	3.80	0.377	0.0132	4.38	0.0112	175.62/224
A0754	T+IC	$3.96^{+0.33}_{-0.35}$	$0.416^{+0.124}_{-0.108}$	$0.0220^{+0.0032}_{-0.0038}$		< 0.0019	174.70/225
	1T	$9.19^{+0.33}_{-0.32}$	$0.273^{+0.032}_{-0.032}$	$0.0699^{+0.0007}_{-0.0007}$			797.01/960
	2T	7.58	0.288	0.0504	15.37	0.0209	783.61/958
HydraA	T+IC	$9.26^{+0.34}_{-0.34}$	$0.292^{+0.034}_{-0.036}$	$0.0668^{+0.0035}_{-0.0034}$		< 0.0023	790.98/959
	1T	$3.98^{+0.09}_{-0.09}$	$0.286^{+0.026}_{-0.025}$	$0.0453^{+0.0007}_{-0.0007}$			607.52/718
	2T	2.72	0.325	0.0290	6.51	0.0181	590.83/716
A1060	T+IC	$3.77^{+0.16}_{-0.17}$	$0.338^{+0.049}_{-0.042}$	$0.0390^{+0.0035}_{-0.0034}$		$0.0020^{+0.0010}_{-0.0011}$	598.26/717
	1T	$3.20^{+0.05}_{-0.05}$	$0.404^{+0.023}_{-0.023}$	$0.0589^{+0.0007}_{-0.0007}$			858.66/972
	2T	3.29	0.404	0.0304	3.12	0.0285	858.63/970
A1367	T+IC	$3.07^{+0.11}_{-0.08}$	$0.458^{+0.040}_{-0.047}$	$0.0539^{+0.0037}_{-0.0027}$		$0.0017^{+0.0008}_{-0.0011}$	850.39/971
	1T	$3.77^{+0.12}_{-0.12}$	$0.299^{+0.037}_{-0.037}$	$0.0326^{+0.0007}_{-0.0006}$			481.37/603
	2T	1.28	0.307	0.0081	4.31	0.0273	472.10/601
MKW4	T+IC	$3.39^{+0.31}_{-0.17}$	$0.398^{+0.074}_{-0.089}$	$0.0254^{+0.0043}_{-0.0025}$		$0.0023^{+0.0008}_{-0.0014}$	471.44/602
	1T	$1.68^{+0.11}_{-0.11}$	$0.634^{+0.239}_{-0.188}$	$0.0153^{+0.0025}_{-0.0021}$			61.30/106
	2T	1.73	0.635	0.0123	1.49	0.0030	61.32/104
	T+IC	$1.68^{+0.11}_{-0.17}$	$0.668^{+0.255}_{-0.192}$	$0.0148^{+0.0024}_{-0.0026}$		< 0.0004	56.17/105

TABLE 5 — *Continued*

Name	Model ^a	Component 1			Component 2		χ^2/dof
		kT (keV)	abund Z_\odot	Norm. ^b (cm^{-5})	kT (keV)	Norm. ^c	
ZwCl1215	1T	$7.12^{+0.34}_{-0.33}$	$0.284^{+0.038}_{-0.037}$	$0.0255^{+0.0004}_{-0.0004}$	8.20	0.0199	465.57/612
	2T	4.23	0.304	0.0060			464.24/610
	T+IC	$7.27^{+0.37}_{-0.37}$	$0.319^{+0.050}_{-0.066}$	$0.0229^{+0.0029}_{-0.0026}$			463.19/611
NGC4636	1T	$0.92^{+0.09}_{-0.09}$	$0.977^{+0.630}_{-0.322}$	$0.0056^{+0.0017}_{-0.0016}$	0.75	0.0039	229.06/363
	2T	26.36	1.988	0.0003			212.46/361
	T+IC	$0.75^{+0.06}_{-0.06}$	$4.985^{+-4.985}_{-2.829}$	$0.0016^{+0.0021}_{-0.0003}$			213.53/362
A3526	1T	$3.95^{+0.03}_{-0.09}$	$0.544^{+0.013}_{-0.015}$	$0.1109^{+0.0025}_{-0.0037}$	4.16	0.0513	2020.73/1762
	2T	3.95	0.544	0.0507			2129.81/1760
	T+IC	$4.00^{+0.05}_{-0.07}$	$0.541^{+0.012}_{-0.011}$	$0.1021^{+0.0011}_{-0.0047}$			2089.03/1761
A1644	1T	$5.14^{+0.24}_{-0.23}$	$0.294^{+0.046}_{-0.045}$	$0.0442^{+0.0011}_{-0.0011}$	7.01	0.0198	394.74/534
	2T	4.00	0.312	0.0249			390.98/532
	T+IC	$5.09^{+0.26}_{-0.26}$	$0.318^{+0.054}_{-0.049}$	$0.0405^{+0.0043}_{-0.0048}$			392.98/533
A1650	1T	$5.94^{+0.17}_{-0.16}$	$0.394^{+0.026}_{-0.026}$	$0.0275^{+0.0003}_{-0.0003}$	7.57	0.0126	755.89/919
	2T	4.83	0.413	0.0151			752.04/917
	T+IC	$5.93^{+0.19}_{-0.19}$	$0.451^{+0.075}_{-0.059}$	$0.0237^{+0.0032}_{-0.0033}$			749.07/918
A1651	1T	$6.45^{+0.36}_{-0.35}$	$0.389^{+0.057}_{-0.056}$	$0.0347^{+0.0009}_{-0.0009}$	7.02	0.0302	212.15/335
	2T	3.41	0.406	0.0049			211.76/333
	T+IC	$6.46^{+0.44}_{-0.42}$	$0.501^{+0.123}_{-0.096}$	$0.0268^{+0.0043}_{-0.0043}$			202.64/334
Coma	1T	$8.51^{+0.11}_{-0.11}$	$0.248^{+0.015}_{-0.015}$	$0.2434^{+0.0013}_{-0.0013}$	9.29	0.1573	1801.39/2167
	2T	7.36	0.248	0.0869			1797.98/2165
	T+IC	$8.51^{+0.11}_{-0.11}$	$0.249^{+0.015}_{-0.015}$	$0.2429^{+0.0017}_{-0.0038}$			1801.47/2166
NGC5044	1T	$1.20^{+0.04}_{-0.04}$	$0.800^{+0.151}_{-0.126}$	$0.0245^{+0.0029}_{-0.0027}$	6.96	0.0009	391.89/497
	2T	1.09	0.866	0.0237			382.01/495
	T+IC	$1.10^{+0.07}_{-0.10}$	$0.943^{+0.251}_{-0.181}$	$0.0218^{+0.0035}_{-0.0035}$			381.79/496
A3558	1T	$5.90^{+0.10}_{-0.10}$	$0.324^{+0.015}_{-0.015}$	$0.0663^{+0.0005}_{-0.0005}$	7.31	0.0226	1282.65/1465
	2T	5.27	0.330	0.0440			1282.28/1463
	T+IC	$5.90^{+0.11}_{-0.10}$	$0.350^{+0.016}_{-0.025}$	$0.0610^{+0.0040}_{-0.0040}$			1277.75/1464
A3562	1T	$5.07^{+0.61}_{-0.55}$	$0.406^{+0.150}_{-0.142}$	$0.0176^{+0.0010}_{-0.0010}$	5.00	0.0091	59.05/134
	2T	5.08	0.414	0.0085			58.81/132
	T+IC	$5.11^{+0.62}_{-0.54}$	$0.398^{+0.155}_{-0.141}$	$0.0176^{+0.0011}_{-0.0039}$			59.51/133
A3571	1T	$7.20^{+0.14}_{-0.14}$	$0.372^{+0.019}_{-0.019}$	$0.1105^{+0.0008}_{-0.0008}$	7.19	0.0762	1621.68/1883
	2T	7.22	0.372	0.0343			1621.68/1881
	T+IC	$7.20^{+0.15}_{-0.15}$	$0.388^{+0.024}_{-0.027}$	$0.1065^{+0.0043}_{-0.0038}$			1621.82/1882
A1795	1T	$5.63^{+0.08}_{-0.08}$	$0.365^{+0.013}_{-0.013}$	$0.0794^{+0.0005}_{-0.0005}$	6.63	0.0479	1741.93/1916
	2T	4.33	0.383	0.0325			1671.68/1914
	T+IC	$5.62^{+0.08}_{-0.09}$	$0.390^{+0.014}_{-0.014}$	$0.0753^{+0.0030}_{-0.0033}$			1674.47/1915
A3581	1T	$1.88^{+0.04}_{-0.04}$	$0.557^{+0.059}_{-0.055}$	$0.0272^{+0.0010}_{-0.0010}$	17.23	0.0012	428.73/555
	2T	1.74	0.571	0.0265			413.71/553
	T+IC	$1.74^{+0.06}_{-0.07}$	$0.625^{+0.079}_{-0.071}$	$0.0243^{+0.0016}_{-0.0016}$			412.74/554
MKW8	1T	$3.35^{+0.29}_{-0.21}$	$0.354^{+0.100}_{-0.093}$	$0.0134^{+0.0007}_{-0.0007}$	5.45	0.0050	160.18/230
	2T	2.42	0.370	0.0088			157.94/228
	T+IC	$3.00^{+0.41}_{-0.41}$	$0.488^{+0.199}_{-0.162}$	$0.0103^{+0.0024}_{-0.0030}$			157.59/229
A2029	1T	$8.01^{+0.21}_{-0.21}$	$0.428^{+0.029}_{-0.029}$	$0.0780^{+0.0008}_{-0.0008}$	8.48	0.0752	877.70/952
	2T	0.29	0.458	0.5676			844.34/950
	T+IC	$8.13^{+0.24}_{-0.23}$	$0.501^{+0.052}_{-0.046}$	$0.0675^{+0.0044}_{-0.0044}$			861.38/951
A2052	1T	$3.01^{+0.05}_{-0.05}$	$0.498^{+0.029}_{-0.029}$	$0.0479^{+0.0006}_{-0.0006}$	3.24	0.0229	723.70/858
	2T	2.80	0.505	0.0250			716.70/856
	T+IC	$2.81^{+0.11}_{-0.10}$	$0.610^{+0.066}_{-0.065}$	$0.0417^{+0.0030}_{-0.0026}$			704.61/857
MKW3S	1T	$3.36^{+0.06}_{-0.06}$	$0.385^{+0.027}_{-0.026}$	$0.0396^{+0.0006}_{-0.0006}$	2.89	0.0208	722.14/847
	2T	3.95	0.389	0.0191			720.11/845
	T+IC	$3.23^{+0.10}_{-0.15}$	$0.433^{+0.051}_{-0.038}$	$0.0361^{+0.0023}_{-0.0033}$			716.12/846
A2065	1T	$6.46^{+0.53}_{-0.47}$	$0.261^{+0.077}_{-0.076}$	$0.0292^{+0.0009}_{-0.0009}$	7.04	0.0224	166.22/258
	2T	4.73	0.268	0.0069			166.19/256
	T+IC	$6.44^{+0.55}_{-0.49}$	$0.274^{+0.088}_{-0.083}$	$0.0278^{+0.0021}_{-0.0038}$			166.41/257
A2063	1T	$4.32^{+0.15}_{-0.12}$	$0.345^{+0.033}_{-0.033}$	$0.0371^{+0.0007}_{-0.0006}$	4.62	0.0173	649.81/783
	2T	4.07	0.345	0.0199			655.50/781
	T+IC	$4.21^{+0.20}_{-0.15}$	$0.380^{+0.055}_{-0.063}$	$0.0348^{+0.0027}_{-0.0041}$			653.90/782
A2142	1T	$10.26^{+0.83}_{-0.74}$	$0.202^{+0.318}_{-0.202}$	$0.0629^{+0.0042}_{-0.0042}$	64.00	0.0032	47.02/98
	2T	9.10	0.224	0.0619			42.08/96
	T+IC	$9.54^{+1.00}_{-1.04}$	< 0.615	$0.0561^{+0.0068}_{-0.0068}$			42.63/97
A2147	1T	$4.99^{+0.66}_{-0.53}$	$0.250^{+0.126}_{-0.120}$	$0.0412^{+0.0023}_{-0.0023}$	6.84	0.0153	104.01/159
	2T	4.18	0.259	0.0261			103.33/157

TABLE 5 — *Continued*

Name	Model ^a	Component 1			Component 2		χ^2/dof
		kT (keV)	abund Z_\odot	Norm. ^b (cm^{-5})	kT (keV)	Norm. ^c	
A2199	T+IC	$5.02^{+0.68}_{-0.53}$	$0.246^{+0.120}_{-0.118}$	$0.0415^{+0.0024}_{-0.0043}$		< 0.0013	104.08/158
	1T	$4.45^{+0.09}_{-0.09}$	$0.363^{+0.021}_{-0.020}$	$0.1019^{+0.0011}_{-0.0011}$			918.41/1078
	2T	2.66	0.382	0.0235	5.01	0.0803	911.87/1076
A2204	T+IC	$4.41^{+0.10}_{-0.11}$	$0.375^{+0.024}_{-0.023}$	$0.0986^{+0.0036}_{-0.0040}$		< 0.0024	916.19/1077
	1T	$7.10^{+0.24}_{-0.23}$	$0.397^{+0.029}_{-0.028}$	$0.0467^{+0.0006}_{-0.0006}$			628.73/781
	2T	4.21	0.494	0.0255	12.93	0.0232	608.41/779
A2256	T+IC	$7.15^{+0.27}_{-0.27}$	$0.487^{+0.078}_{-0.063}$	$0.0380^{+0.0048}_{-0.0047}$		$0.0025^{+0.0013}_{-0.0014}$	619.76/780
	1T	$6.99^{+0.34}_{-0.38}$	$0.301^{+0.045}_{-0.044}$	$0.0526^{+0.0011}_{-0.0009}$			341.67/443
	2T	0.40	0.326	0.1181	7.59	0.0504	326.25/441
A2255	T+IC	$6.94^{+0.36}_{-0.35}$	$0.324^{+0.049}_{-0.047}$	$0.0488^{+0.0032}_{-0.0032}$		$0.0013^{+0.0011}_{-0.0011}$	337.34/442
	1T	$7.43^{+0.80}_{-0.71}$	$0.269^{+0.107}_{-0.104}$	$0.0237^{+0.0008}_{-0.0008}$			104.15/193
	2T	6.84	0.268	0.0130	8.21	0.0107	104.16/191
A3667	T+IC	$7.41^{+0.86}_{-0.67}$	$0.263^{+0.111}_{-0.096}$	$0.0238^{+0.0008}_{-0.0018}$		< 0.0005	103.80/192
	1T	$6.60^{+0.11}_{-0.11}$	$0.268^{+0.015}_{-0.015}$	$0.0758^{+0.0005}_{-0.0005}$			1497.45/1652
	2T	5.07	0.286	0.0425	9.35	0.0343	1485.95/1650
S1101	T+IC	$6.70^{+0.12}_{-0.13}$	$0.304^{+0.023}_{-0.026}$	$0.0658^{+0.0046}_{-0.0035}$		$0.0032^{+0.0011}_{-0.0015}$	1482.95/1651
	1T	$2.65^{+0.06}_{-0.06}$	$0.336^{+0.038}_{-0.037}$	$0.0259^{+0.0006}_{-0.0006}$			418.31/534
	2T	1.83	0.331	0.0101	3.12	0.0168	414.11/532
A2589	T+IC	$2.56^{+0.12}_{-0.12}$	$0.363^{+0.052}_{-0.048}$	$0.0249^{+0.0013}_{-0.0015}$		< 0.0007	414.49/533
	1T	$3.69^{+0.13}_{-0.12}$	$0.543^{+0.052}_{-0.050}$	$0.0205^{+0.0004}_{-0.0004}$			335.38/446
	2T	0.35	0.554	0.0396	3.87	0.0195	326.42/444
A2597	T+IC	$3.33^{+0.22}_{-0.20}$	$0.762^{+0.198}_{-0.144}$	$0.0154^{+0.0026}_{-0.0025}$		$0.0015^{+0.0007}_{-0.0007}$	325.13/445
	1T	$3.36^{+0.07}_{-0.07}$	$0.329^{+0.024}_{-0.024}$	$0.0274^{+0.0004}_{-0.0004}$			626.72/721
	2T	2.29	0.360	0.0178	5.43	0.0109	600.23/719
A2634	T+IC	$2.95^{+0.15}_{-0.17}$	$0.473^{+0.085}_{-0.066}$	$0.0211^{+0.0021}_{-0.0022}$		$0.0018^{+0.0005}_{-0.0006}$	598.61/720
	1T	$4.50^{+0.56}_{-0.45}$	$0.292^{+0.148}_{-0.140}$	$0.0182^{+0.0011}_{-0.0010}$			108.16/140
	2T	4.55	0.292	0.0092	4.46	0.0091	108.16/138
A2657	T+IC	$4.54^{+0.56}_{-0.48}$	$0.275^{+0.142}_{-0.127}$	$0.0184^{+0.0006}_{-0.0032}$		< 0.0010	107.58/139
	1T	$5.14^{+0.30}_{-0.28}$	$0.284^{+0.065}_{-0.063}$	$0.0256^{+0.0008}_{-0.0007}$			273.87/356
	2T	2.16	0.383	0.0112	7.83	0.0165	263.96/354
A4038	T+IC	$5.15^{+0.30}_{-0.29}$	$0.284^{+0.066}_{-0.063}$	$0.0256^{+0.0008}_{-0.0032}$		< 0.0010	273.84/355
	1T	$3.17^{+0.05}_{-0.05}$	$0.371^{+0.025}_{-0.024}$	$0.0593^{+0.0008}_{-0.0008}$			870.11/1058
	2T	2.54	0.384	0.0416	4.83	0.0190	858.73/1056
A4059	T+IC	$3.02^{+0.10}_{-0.10}$	$0.426^{+0.048}_{-0.042}$	$0.0538^{+0.0032}_{-0.0032}$		$0.0017^{+0.0009}_{-0.0009}$	861.42/1057
	1T	$4.23^{+0.13}_{-0.12}$	$0.428^{+0.036}_{-0.035}$	$0.0341^{+0.0006}_{-0.0006}$			480.11/694
	2T	2.66	0.443	0.0072	4.71	0.0273	478.71/692
	T+IC	$4.23^{+0.13}_{-0.14}$	$0.428^{+0.050}_{-0.035}$	$0.0341^{+0.0006}_{-0.0028}$		< 0.0009	480.14/693

^a Parameters for the 2T model are unconstrained.

^b Normalization of the APEC thermal spectrum, which is given by $\{10^{-14}/[4\pi(1+z)^2 D_A^2]\} \int n_e n_H dV$, where z is the redshift, D_A is the angular diameter distance, n_e is the electron density, n_H is the ionized hydrogen density, and V is the volume of the cluster.

^c Value is the normalization of the power-law component for the T+IC model, which is the photon flux at a photon energy of 1 keV in units of photons $\text{cm}^{-2} \text{s}^{-1} \text{keV}^{-1}$. For the 2T model, the value is the normalization of the second APEC thermal model in units of cm^{-5} .

TABLE 6
JOINT THERMAL AND NON-THERMAL FITS TO THE EPIC AND BAT SPECTRA
(3–195 keV)

Name	Model ^a	Component 1			Component 2		χ^2/dof
		kT (keV)	abund Z_\odot	Norm. ^b (cm^{-5})	kT (keV)	Norm. ^c	
A0085	1T	$6.94^{+0.31}_{-0.26}$	$0.363^{+0.034}_{-0.033}$	$0.0746^{+0.0016}_{-0.0015}$			410.01/534
	2T	6.90	0.364	0.0449	7.01	0.0298	410.28/532
A0119	T+IC	$6.91^{+0.30}_{-0.27}$	$0.362^{+0.037}_{-0.030}$	$0.0746^{+0.0015}_{-0.0022}$		< 0.0007	411.40/533
	1T	$6.71^{+0.87}_{-0.79}$	$0.243^{+0.082}_{-0.080}$	$0.0285^{+0.0020}_{-0.0015}$			115.75/162
	2T	6.78	0.246	0.0158	6.59	0.0127	115.65/160
A0133	T+IC	$6.73^{+0.88}_{-0.80}$	$0.242^{+0.087}_{-0.076}$	$0.0286^{+0.0020}_{-0.0028}$		< 0.0009	115.69/161
	1T	$4.27^{+0.34}_{-0.27}$	$0.442^{+0.053}_{-0.051}$	$0.0211^{+0.0012}_{-0.0011}$			134.52/237
	2T	2.10	0.442	0.0003	4.34	0.0207	134.60/235
	T+IC	$4.03^{+0.59}_{-0.35}$	$0.462^{+0.134}_{-0.068}$	$0.0204^{+0.0019}_{-0.0039}$		< 0.0016	134.21/236

TABLE 6 — *Continued*

Name	Model ^a	Component 1			Component 2		χ^2/dof
		kT (keV)	abund Z_\odot	Norm. ^b (cm^{-5})	kT (keV)	Norm. ^c	
NGC507	1T	$1.85^{+0.35}_{-0.27}$	$0.829^{+0.757}_{-0.431}$	$0.0073^{+0.0029}_{-0.0019}$	64.00	0.0005	64.52/99
	2T	1.60	1.003	0.0069			62.13/97
	T+IC	$1.61^{+0.44}_{-0.40}$	$1.434^{+-1.434}_{-0.924}$	$0.0052^{+0.0044}_{-0.0036}$			62.87/98
A0262	1T	$2.33^{+0.09}_{-0.08}$	$0.412^{+0.059}_{-0.055}$	$0.0531^{+0.0027}_{-0.0026}$	2.54	0.0051	297.16/379
	2T	2.31	0.412	0.0480			297.16/377
	T+IC	$2.33^{+0.10}_{-0.09}$	$0.403^{+0.065}_{-0.048}$	$0.0535^{+0.0025}_{-0.0029}$			297.48/378
A0400	1T	$2.34^{+0.30}_{-0.23}$	$0.352^{+0.168}_{-0.143}$	$0.0195^{+0.0031}_{-0.0027}$	2.22	0.0107	138.40/159
	2T	2.49	0.352	0.0087			138.42/157
	T+IC	$2.42^{+0.25}_{-0.31}$	$0.346^{+0.163}_{-0.141}$	$0.0196^{+0.0032}_{-0.0027}$			137.80/158
A0399	1T	$7.63^{+0.71}_{-0.67}$	$0.233^{+0.058}_{-0.056}$	$0.0349^{+0.0014}_{-0.0014}$	7.62	0.0244	152.92/229
	2T	7.67	0.233	0.0105			152.92/227
	T+IC	$7.69^{+0.63}_{-0.76}$	$0.235^{+0.057}_{-0.057}$	$0.0347^{+0.0016}_{-0.0019}$			153.07/228
A3112	1T	$5.29^{+0.27}_{-0.22}$	$0.455^{+0.032}_{-0.031}$	$0.0339^{+0.0011}_{-0.0011}$	15.19	0.0073	374.66/448
	2T	4.03	0.550	0.0284			364.14/446
	T+IC	$5.10^{+0.29}_{-0.24}$	$0.527^{+0.066}_{-0.056}$	$0.0296^{+0.0032}_{-0.0028}$			367.28/447
Fornax	1T	$2.01^{+0.17}_{-0.13}$	$0.253^{+0.096}_{-0.085}$	$0.0192^{+0.0022}_{-0.0021}$	3.40	0.0038	471.90/503
	2T	1.60	0.254	0.0177			470.55/501
	T+IC	$1.57^{+0.25}_{-0.28}$	$0.488^{+0.408}_{-0.179}$	$0.0176^{+0.0036}_{-0.0044}$			465.05/502
2A0335	1T	$3.22^{+0.13}_{-0.12}$	$0.400^{+0.036}_{-0.035}$	$0.0941^{+0.0037}_{-0.0037}$	3.93	0.0407	254.73/381
	2T	2.67	0.411	0.0553			254.16/379
	T+IC	$3.22^{+0.13}_{-0.13}$	$0.399^{+0.040}_{-0.032}$	$0.0943^{+0.0036}_{-0.0042}$			254.74/380
IIIZw54	1T	$3.04^{+0.28}_{-0.23}$	$0.242^{+0.068}_{-0.063}$	$0.0170^{+0.0015}_{-0.0015}$	3.07	0.0081	156.99/228
	2T	3.01	0.242	0.0089			156.99/226
	T+IC	$2.81^{+0.50}_{-0.41}$	$0.280^{+0.130}_{-0.101}$	$0.0159^{+0.0025}_{-0.0025}$			157.91/227
A3158	1T	$6.34^{+0.55}_{-0.52}$	$0.348^{+0.063}_{-0.061}$	$0.0388^{+0.0019}_{-0.0019}$	5.91	0.0214	154.76/217
	2T	6.83	0.348	0.0173			154.52/215
	T+IC	$6.32^{+0.54}_{-0.55}$	$0.350^{+0.066}_{-0.061}$	$0.0387^{+0.0020}_{-0.0030}$			154.81/216
NGC1550	1T	$1.55^{+0.19}_{-0.14}$	$0.299^{+0.212}_{-0.163}$	$0.0285^{+0.0075}_{-0.0061}$	1.53	0.0141	81.90/128
	2T	1.56	0.299	0.0145			82.39/126
	T+IC	$1.31^{+0.36}_{-0.30}$	$0.390^{+0.442}_{-0.223}$	$0.0305^{+0.0151}_{-0.0096}$			81.43/127
EXO0422	1T	$3.21^{+0.15}_{-0.13}$	$0.336^{+0.035}_{-0.034}$	$0.0289^{+0.0013}_{-0.0013}$	3.62	0.0142	330.67/446
	2T	2.80	0.340	0.0150			330.65/444
	T+IC	$3.06^{+0.25}_{-0.37}$	$0.372^{+0.128}_{-0.061}$	$0.0276^{+0.0023}_{-0.0036}$			329.39/445
A3266	1T	$8.48^{+0.45}_{-0.35}$	$0.196^{+0.032}_{-0.031}$	$0.0790^{+0.0016}_{-0.0015}$	8.95	0.0640	564.78/730
	2T	6.85	0.195	0.0151			564.31/728
	T+IC	$8.41^{+0.44}_{-0.36}$	$0.199^{+0.032}_{-0.032}$	$0.0770^{+0.0033}_{-0.0036}$			564.43/729
A0496	1T	$4.59^{+0.14}_{-0.13}$	$0.388^{+0.022}_{-0.022}$	$0.0805^{+0.0016}_{-0.0016}$	5.03	0.0287	631.47/766
	2T	4.35	0.388	0.0519			631.48/764
	T+IC	$4.59^{+0.16}_{-0.12}$	$0.386^{+0.023}_{-0.021}$	$0.0806^{+0.0013}_{-0.0023}$			630.73/765
A3376	1T	$5.77^{+1.12}_{-0.95}$	$0.450^{+0.146}_{-0.129}$	$0.0086^{+0.0010}_{-0.0008}$	6.83	0.0070	63.94/84
	2T	1.98	0.523	0.0025			63.31/82
	T+IC	$5.25^{+1.33}_{-1.31}$	$0.630^{+0.661}_{-0.217}$	$0.0066^{+0.0028}_{-0.0032}$			63.24/83
A3391	1T	$6.85^{+0.59}_{-0.46}$	$0.314^{+0.054}_{-0.052}$	$0.0200^{+0.0008}_{-0.0007}$	6.87	0.0112	202.73/303
	2T	6.83	0.314	0.0088			202.75/301
	T+IC	$6.75^{+0.57}_{-0.56}$	$0.353^{+0.071}_{-0.083}$	$0.0178^{+0.0028}_{-0.0027}$			203.22/302
A3395s	1T	$6.03^{+1.29}_{-1.09}$	$0.240^{+0.109}_{-0.101}$	$0.0076^{+0.0010}_{-0.0007}$	7.64	0.0039	56.82/124
	2T	4.31	0.258	0.0039			56.24/122
	T+IC	$5.88^{+1.48}_{-0.69}$	$0.269^{+0.154}_{-0.134}$	$0.0067^{+0.0019}_{-0.0020}$			56.82/123
R1504	1T	$8.32^{+0.71}_{-0.56}$	$0.407^{+0.055}_{-0.051}$	$0.0495^{+0.0020}_{-0.0019}$	9.48	0.0299	940.16/788
	2T	6.93	0.412	0.0198			939.83/786
	T+IC	$11.45^{+1.28}_{-0.99}$	$0.444^{+0.094}_{-0.077}$	$0.0473^{+0.0014}_{-0.0043}$			1014.97/787
A0576	1T	$4.37^{+0.61}_{-0.54}$	$0.363^{+0.088}_{-0.083}$	$0.0231^{+0.0026}_{-0.0019}$	6.37	0.0113	91.85/129
	2T	2.72	0.430	0.0136			90.65/127
	T+IC	$4.16^{+0.74}_{-0.59}$	$0.402^{+0.125}_{-0.109}$	$0.0216^{+0.0037}_{-0.0039}$			90.96/128
A0754	1T	$9.46^{+0.43}_{-0.42}$	$0.286^{+0.034}_{-0.033}$	$0.0696^{+0.0011}_{-0.0011}$	16.61	0.0143	528.60/645
	2T	8.13	0.288	0.0564			529.13/643
	T+IC	$9.40^{+0.43}_{-0.42}$	$0.284^{+0.038}_{-0.033}$	$0.0695^{+0.0011}_{-0.0043}$			531.98/644
HydraA	1T	$4.39^{+0.19}_{-0.18}$	$0.282^{+0.026}_{-0.026}$	$0.0414^{+0.0014}_{-0.0013}$	6.84	0.0079	330.74/443
	2T	3.89	0.297	0.0343			330.58/441
	T+IC	$4.32^{+0.25}_{-0.24}$	$0.293^{+0.038}_{-0.035}$	$0.0399^{+0.0028}_{-0.0031}$			330.55/442
A1060	1T	$3.43^{+0.09}_{-0.09}$	$0.383^{+0.025}_{-0.023}$	$0.0558^{+0.0016}_{-0.0012}$	3.42	0.0268	519.24/641
	2T	3.43	0.383	0.0290			519.24/639

TABLE 6 — *Continued*

Name	Model ^a	Component 1			Component 2		χ^2/dof
		kT (keV)	abund Z_{\odot}	Norm. ^b (cm^{-5})	kT (keV)	Norm. ^c	
A1367	T+IC	$3.42^{+0.09}_{-0.10}$	$0.384^{+0.029}_{-0.022}$	$0.0559^{+0.0015}_{-0.0021}$		< 0.0006	522.27/640
	1T	$4.17^{+0.26}_{-0.23}$	$0.298^{+0.040}_{-0.039}$	$0.0297^{+0.0015}_{-0.0014}$			259.15/344
	2T	1.05	0.302	0.0052	4.32	0.0283	258.74/342
MKW4	T+IC	$3.93^{+0.32}_{-0.34}$	$0.349^{+0.063}_{-0.058}$	$0.0262^{+0.0031}_{-0.0032}$		$0.0013^{+0.0011}_{-0.0011}$	254.94/343
	1T	$1.73^{+0.28}_{-0.26}$	$0.886^{+1.045}_{-0.514}$	$0.0124^{+0.0065}_{-0.0040}$			27.27/48
	2T	1.73	0.822	0.0126	0.71	0.0000	27.43/46
ZwCl1215	T+IC	$1.67^{+0.33}_{-0.42}$	$0.984^{+0.984}_{-0.601}$	$0.0119^{+0.0069}_{-0.0080}$		< 0.0007	27.21/47
	1T	$7.64^{+0.51}_{-0.50}$	$0.299^{+0.043}_{-0.042}$	$0.0247^{+0.0008}_{-0.0007}$			279.58/372
	2T	6.83	0.302	0.0044	7.83	0.0203	278.15/370
NGC4636	T+IC	$7.63^{+0.54}_{-0.48}$	$0.300^{+0.049}_{-0.040}$	$0.0248^{+0.0007}_{-0.0022}$		< 0.0008	278.15/371
	1T	$2.30^{+3.13}_{-1.02}$	$0.197^{+4.127}_{-0.197}$	$0.0019^{+0.0033}_{-0.0019}$			101.60/154
	2T	17.23	1.654	0.0004	0.72	0.0036	99.60/152
A3526	T+IC	$0.37^{+2.82}_{-0.31}$	< 0.000	$0.0252^{+173.0428}_{-0.0243}$		< 0.0003	99.45/153
	1T	$3.75^{+0.13}_{-0.04}$	$0.532^{+0.013}_{-0.013}$	$0.1184^{+0.0028}_{-0.0059}$			1487.12/1496
	2T	4.05	0.512	0.0562	3.78	0.0563	1486.08/1494
A1644	T+IC	$3.93^{+0.11}_{-0.05}$	$0.511^{+0.010}_{-0.017}$	$0.1121^{+0.0016}_{-0.0040}$		< 0.0005	1493.02/1495
	1T	$5.74^{+0.49}_{-0.54}$	$0.301^{+0.051}_{-0.049}$	$0.0411^{+0.0024}_{-0.0018}$			231.49/305
	2T	4.36	0.314	0.0205	6.85	0.0219	229.61/303
A1650	T+IC	$5.69^{+0.53}_{-0.60}$	$0.309^{+0.062}_{-0.055}$	$0.0400^{+0.0034}_{-0.0048}$		< 0.0022	231.32/304
	1T	$6.12^{+0.25}_{-0.25}$	$0.399^{+0.029}_{-0.028}$	$0.0270^{+0.0007}_{-0.0007}$			454.08/603
	2T	5.45	0.405	0.0189	7.87	0.0082	453.97/601
A1651	T+IC	$5.96^{+0.40}_{-0.27}$	$0.411^{+0.096}_{-0.040}$	$0.0260^{+0.0017}_{-0.0047}$		< 0.0019	453.35/602
	1T	$6.94^{+0.62}_{-0.63}$	$0.411^{+0.068}_{-0.064}$	$0.0331^{+0.0019}_{-0.0013}$			133.74/199
	2T	5.40	0.414	0.0035	7.13	0.0297	133.53/197
Coma	T+IC	$6.48^{+0.69}_{-0.65}$	$0.495^{+0.123}_{-0.095}$	$0.0273^{+0.0043}_{-0.0044}$		$0.0022^{+0.0015}_{-0.0015}$	128.72/198
	1T	$8.59^{+0.17}_{-0.14}$	$0.249^{+0.015}_{-0.015}$	$0.2435^{+0.0021}_{-0.0019}$			1454.06/1835
	2T	8.33	0.249	0.0923	8.77	0.1514	1453.89/1833
NGC5044	T+IC	$8.58^{+0.18}_{-0.14}$	$0.248^{+0.015}_{-0.015}$	$0.2436^{+0.0021}_{-0.0027}$		< 0.0009	1454.15/1834
	1T	$1.44^{+0.17}_{-0.15}$	$0.685^{+0.540}_{-0.328}$	$0.0184^{+0.0067}_{-0.0048}$			179.51/238
	2T	1.43	0.688	0.0185	0.03	0.0000	179.48/236
A3558	T+IC	$1.37^{+0.22}_{-0.28}$	$0.801^{+1.701}_{-0.435}$	$0.0174^{+0.0080}_{-0.0073}$		< 0.0006	180.08/237
	1T	$6.22^{+0.15}_{-0.15}$	$0.334^{+0.016}_{-0.016}$	$0.0643^{+0.0009}_{-0.0009}$			911.87/1133
	2T	5.97	0.334	0.0423	6.71	0.0220	911.85/1131
A3562	T+IC	$6.23^{+0.14}_{-0.16}$	$0.335^{+0.016}_{-0.016}$	$0.0642^{+0.0010}_{-0.0019}$		< 0.0007	911.80/1132
	1T	$5.41^{+1.22}_{-0.97}$	$0.405^{+0.158}_{-0.146}$	$0.0168^{+0.0024}_{-0.0018}$			29.73/78
	2T	5.39	0.413	0.0081	5.34	0.0087	29.58/76
A3571	T+IC	$5.24^{+1.29}_{-0.88}$	$0.415^{+0.182}_{-0.146}$	$0.0170^{+0.0022}_{-0.0038}$		< 0.0012	29.59/77
	1T	$7.41^{+0.19}_{-0.19}$	$0.381^{+0.021}_{-0.020}$	$0.1089^{+0.0013}_{-0.0013}$			1281.49/1551
	2T	7.39	0.381	0.0336	7.42	0.0753	1281.48/1549
A1795	T+IC	$7.44^{+0.21}_{-0.18}$	$0.380^{+0.022}_{-0.019}$	$0.1091^{+0.0012}_{-0.0023}$		< 0.0008	1278.53/1550
	1T	$5.87^{+0.12}_{-0.12}$	$0.376^{+0.014}_{-0.014}$	$0.0778^{+0.0009}_{-0.0009}$			1344.31/1584
	2T	4.49	0.382	0.0252	6.49	0.0537	1345.49/1582
A3581	T+IC	$5.85^{+0.12}_{-0.11}$	$0.376^{+0.017}_{-0.014}$	$0.0779^{+0.0009}_{-0.0026}$		< 0.0009	1346.85/1583
	1T	$2.00^{+0.11}_{-0.10}$	$0.419^{+0.086}_{-0.078}$	$0.0272^{+0.0023}_{-0.0022}$			200.26/287
	2T	1.83	0.473	0.0273	13.54	0.0009	198.23/285
MKW8	T+IC	$1.82^{+0.24}_{-0.13}$	$0.530^{+0.153}_{-0.161}$	$0.0255^{+0.0033}_{-0.0027}$		< 0.0009	198.62/286
	1T	$3.82^{+0.60}_{-0.47}$	$0.321^{+0.104}_{-0.097}$	$0.0121^{+0.0014}_{-0.0013}$			80.29/129
	2T	3.47	0.319	0.0062	4.20	0.0059	80.27/127
A2029	T+IC	$3.53^{+0.84}_{-0.78}$	$0.384^{+0.321}_{-0.160}$	$0.0105^{+0.0029}_{-0.0031}$		< 0.0016	80.21/128
	1T	$8.47^{+0.37}_{-0.28}$	$0.453^{+0.034}_{-0.033}$	$0.0757^{+0.0014}_{-0.0014}$			551.00/641
	2T	7.41	0.457	0.0338	9.55	0.0420	549.99/639
A2052	T+IC	$8.39^{+0.33}_{-0.30}$	$0.482^{+0.046}_{-0.047}$	$0.0711^{+0.0051}_{-0.0044}$		< 0.0033	548.15/640
	1T	$3.21^{+0.10}_{-0.09}$	$0.473^{+0.032}_{-0.031}$	$0.0451^{+0.0014}_{-0.0014}$			430.61/532
	2T	3.22	0.473	0.0236	3.20	0.0216	430.61/530
MKW3S	T+IC	$3.07^{+0.19}_{-0.19}$	$0.519^{+0.080}_{-0.061}$	$0.0429^{+0.0031}_{-0.0034}$		< 0.0019	441.27/531
	1T	$3.64^{+0.13}_{-0.12}$	$0.381^{+0.028}_{-0.028}$	$0.0368^{+0.0011}_{-0.0011}$			420.99/524
	2T	3.81	0.381	0.0181	3.47	0.0187	420.98/522
A2065	T+IC	$3.63^{+0.13}_{-0.23}$	$0.383^{+0.074}_{-0.029}$	$0.0366^{+0.0013}_{-0.0043}$		< 0.0014	420.98/523
	1T	$6.58^{+0.90}_{-0.75}$	$0.260^{+0.080}_{-0.078}$	$0.0289^{+0.0020}_{-0.0017}$			100.40/165
	2T	6.44	0.261	0.0067	6.61	0.0222	100.37/163
A2063	T+IC	$6.53^{+0.92}_{-0.81}$	$0.269^{+0.091}_{-0.083}$	$0.0281^{+0.0027}_{-0.0038}$		< 0.0016	100.19/164
	1T	$4.50^{+0.23}_{-0.21}$	$0.339^{+0.034}_{-0.033}$	$0.0360^{+0.0012}_{-0.0012}$			437.10/519

TABLE 6 — *Continued*

Name	Model ^a	Component 1			Component 2		χ^2/dof
		kT (keV)	abund Z_\odot	Norm. ^b (cm^{-5})	kT (keV)	Norm. ^c	
A2142	2T	4.42	0.344	0.0191	4.65	0.0168	429.73/517
	T+IC	$4.52^{+0.27}_{-0.31}$	$0.344^{+0.049}_{-0.033}$	$0.0360^{+0.0012}_{-0.0038}$		< 0.0013	429.76/518
	1T	$10.41^{+1.03}_{-0.84}$	$0.195^{+0.348}_{-0.195}$	$0.0645^{+0.0061}_{-0.0061}$			27.85/60
	2T	8.95	0.209	0.0634	64.00	0.0035	22.38/58
A2147	T+IC	$9.23^{+1.21}_{-1.24}$	< 0.577	$0.0576^{+0.0073}_{-0.0073}$		$0.0031^{+0.0020}_{-0.0021}$	21.97/59
	1T	$5.62^{+1.14}_{-0.86}$	$0.239^{+0.138}_{-0.128}$	$0.0381^{+0.0044}_{-0.0037}$			56.38/99
	2T	5.55	0.238	0.0234	5.68	0.0147	56.43/97
A2199	T+IC	$5.50^{+1.23}_{-0.77}$	$0.239^{+0.142}_{-0.126}$	$0.0383^{+0.0041}_{-0.0043}$		< 0.0011	56.49/98
	1T	$4.59^{+0.14}_{-0.13}$	$0.367^{+0.022}_{-0.021}$	$0.0994^{+0.0021}_{-0.0021}$			573.33/746
	2T	4.39	0.367	0.0498	4.80	0.0496	573.18/744
A2204	T+IC	$4.57^{+0.16}_{-0.14}$	$0.372^{+0.025}_{-0.025}$	$0.0982^{+0.0031}_{-0.0039}$		< 0.0017	572.92/745
	1T	$7.46^{+0.33}_{-0.32}$	$0.414^{+0.033}_{-0.032}$	$0.0453^{+0.0011}_{-0.0010}$			375.74/507
	2T	5.44	0.458	0.0309	15.49	0.0159	366.89/505
A2256	T+IC	$7.39^{+0.40}_{-0.18}$	$0.450^{+0.058}_{-0.067}$	$0.0442^{+0.0021}_{-0.0067}$		< 0.0025	375.45/506
	1T	$7.91^{+0.48}_{-0.46}$	$0.324^{+0.053}_{-0.051}$	$0.0499^{+0.0015}_{-0.0015}$			199.21/262
	2T	8.58	0.330	0.0213	7.25	0.0286	195.46/260
A2255	T+IC	$7.70^{+0.47}_{-0.46}$	$0.328^{+0.055}_{-0.049}$	$0.0498^{+0.0014}_{-0.0028}$		< 0.0011	194.84/261
	1T	$7.18^{+1.13}_{-0.86}$	$0.256^{+0.108}_{-0.101}$	$0.0242^{+0.0017}_{-0.0016}$			55.90/119
	2T	6.85	0.251	0.0134	7.78	0.0110	55.55/117
A3667	T+IC	$7.16^{+1.26}_{-0.82}$	$0.246^{+0.110}_{-0.094}$	$0.0245^{+0.0016}_{-0.0021}$		< 0.0006	55.81/118
	1T	$7.13^{+0.20}_{-0.20}$	$0.276^{+0.017}_{-0.016}$	$0.0730^{+0.0009}_{-0.0009}$			1148.25/1320
	2T	6.77	0.277	0.0399	7.57	0.0332	1148.23/1318
S1101	T+IC	$7.16^{+0.21}_{-0.19}$	$0.271^{+0.018}_{-0.016}$	$0.0731^{+0.0003}_{-0.0028}$		< 0.0010	1156.48/1319
	1T	$2.85^{+0.14}_{-0.13}$	$0.335^{+0.044}_{-0.042}$	$0.0236^{+0.0012}_{-0.0012}$			213.81/283
	2T	2.16	0.353	0.0166	3.90	0.0088	212.44/281
A2589	T+IC	$2.85^{+0.14}_{-0.24}$	$0.334^{+0.059}_{-0.039}$	$0.0237^{+0.0012}_{-0.0015}$		< 0.0005	214.42/282
	1T	$3.86^{+0.23}_{-0.21}$	$0.545^{+0.055}_{-0.053}$	$0.0197^{+0.0009}_{-0.0009}$			163.53/252
	2T	3.41	0.622	0.0186	52.96	0.0016	157.95/250
A2597	T+IC	$3.43^{+0.40}_{-0.36}$	$0.754^{+0.288}_{-0.179}$	$0.0153^{+0.0033}_{-0.0029}$		$0.0014^{+0.0008}_{-0.0010}$	158.69/251
	1T	$3.89^{+0.17}_{-0.16}$	$0.316^{+0.025}_{-0.025}$	$0.0238^{+0.0009}_{-0.0009}$			310.13/407
	2T	3.43	0.317	0.0124	4.39	0.0114	310.12/405
A2634	T+IC	$3.78^{+0.29}_{-0.31}$	$0.337^{+0.062}_{-0.047}$	$0.0227^{+0.0020}_{-0.0026}$		< 0.0012	310.37/406
	1T	$4.81^{+1.19}_{-0.88}$	$0.266^{+0.140}_{-0.132}$	$0.0180^{+0.0029}_{-0.0023}$			62.69/79
	2T	0.44	0.297	0.4055	5.76	0.0153	61.04/77
A2657	T+IC	$4.84^{+1.12}_{-0.94}$	$0.269^{+0.148}_{-0.131}$	$0.0179^{+0.0030}_{-0.0027}$		< 0.0008	62.73/78
	1T	$5.73^{+0.64}_{-0.60}$	$0.251^{+0.068}_{-0.066}$	$0.0242^{+0.0016}_{-0.0013}$			176.95/235
	2T	2.91	0.267	0.0054	6.45	0.0199	177.03/233
A4038	T+IC	$5.77^{+0.60}_{-0.64}$	$0.252^{+0.067}_{-0.068}$	$0.0241^{+0.0017}_{-0.0021}$		< 0.0007	176.95/234
	1T	$3.39^{+0.12}_{-0.11}$	$0.345^{+0.026}_{-0.025}$	$0.0559^{+0.0019}_{-0.0017}$			579.52/726
	2T	3.07	0.350	0.0298	3.73	0.0267	579.38/724
A4059	T+IC	$3.36^{+0.14}_{-0.18}$	$0.352^{+0.045}_{-0.031}$	$0.0554^{+0.0024}_{-0.0032}$		< 0.0013	579.42/725
	1T	$4.43^{+0.23}_{-0.21}$	$0.428^{+0.037}_{-0.036}$	$0.0329^{+0.0012}_{-0.0011}$			259.39/427
	2T	4.39	0.431	0.0162	4.39	0.0168	261.26/425
	T+IC	$4.44^{+0.22}_{-0.22}$	$0.425^{+0.040}_{-0.033}$	$0.0329^{+0.0013}_{-0.0016}$		< 0.0005	259.32/426

^a Parameters for the 2T model are unconstrained.

^b Normalization of the APEC thermal spectrum, which is given by $\{10^{-14}/[4\pi(1+z)^2 D_A^2]\} \int n_e n_H dV$, where z is the redshift, D_A is the angular diameter distance, n_e is the electron density, n_H is the ionized hydrogen density, and V is the volume of the cluster.

^c Value is the normalization of the power-law component for the T+IC model, which is the photon flux at a photon energy of 1 keV in units of photons $\text{cm}^{-2} \text{s}^{-1} \text{keV}^{-1}$. For the 2T model, the value is the normalization of the second APEC thermal model in units of cm^{-5} .